MODELING OF THE INTERACTION BETWEEN DENSIFICATION MECHANISMS IN POWDER COMPACTION

S. J. Subramanian and P. Sofronis

Department of Theoretical and Applied Mechanics,
University of Illinois at Urbana-Champaign,
216 S. Wright Street, Urbana IL 61801, U.S.A.

May 1999

ABSTRACT

Sinter-forging is a common means of forming ceramic or inter-metallic components for modern technological applications such as advanced structural materials, magnetic materials, thin ceramic layers on substrates and nanocomposites. Micrometer/nanometer-sized powders provide significant advantages in terms of reduced processing pressures/temperatures and increased control over the final mircostructure. Although extensive research in the past twenty years has identified and analyzed the individual mechanisms acting at the microscale during densification, no comparable progress has been made towards understanding the full spectrum of interactions between the mechanisms. In this paper, a micromechanical model of powder consolidation is presented. It accounts for the elastic and power-law creep deformation of the bulk material along with stress-driven diffusion on the interparticle contacts and curvature-driven surface diffusion along the pore surfaces. The finite element method is used to obtain the time-dependent deformation of the powder aggregate from which macroscopic quantities such as relative density, densification rate, and strain rate as well as microscopic quantities such as volumetric flux and pore surface curvature are calculated. Comparisons are made with existing models and experimental data from the consolidation of micron-sized Al_2O_3 and TiAl.

1. INTRODUCTION

Powder processing is used in forming complex shaped components from ceramic or inter-metallic materials. Sinter-forging is an attractive means of producing dense fine-grained components and is especially suited to produce alloys and composites. It is convenient to speak of the consolidation process as occurring in two stages (Ashby, 1974; Helle *et al.*, 1985; Swinkels and Ashby, 1981). Stage I is characterized by connected porosity and existence of discrete necks between individual particles. When the relative density (density of compact/density of fully compact material) is greater than about 0.9, one enters stage II of the deformation, wherein the porosity is isolated with near equilibrium-shaped pores.

The closing of porosity typically occurs by various deformation mechanisms like linear elasticity, rate-independent plasticity, power-law creep and diffusion along the grain-boundaries and pore surfaces, and interparticle slip (Ashby, 1974; Swinkels and Ashby, 1981; Helle *et al.*, 1985). Arzt and coworkers (Arzt, 1982; Arzt *et al.*, 1983; Fischmeister and Arzt, 1983) developed a model for densification that took into account the evolving particle coordination number and contact size during densification. Subsequently, a variety of models have used their idea of an isotropically evolving contact area to predict the macroscopic behavior of a powder compact (Helle *et al.*, 1985; McMeeking and Kuhn, 1992).

Models for stage I densification have been proposed in which the single dominant mechanism is plasticity (Fleck *et al.*, 1992; Akisanya *et al.*, 1994; Akisanya and Cocks, 1995; Fleck, 1995) or power-law creep (Ashby, 1974; Swinkels and Ashby, 1981; Kuhn and McMeeking, 1992; Bouvard, 1993) or grain boundary diffusion (McMeeking and Kuhn, 1992) or interparticle slip (Casagranda and Sofronis, 1997). Cocks (1992) has

suggested a method to include the effect of an interface reaction stress (Ashby, 1969; Burton, 1972) on the diffusion process along the interparticle contacts. Work has also been done in the area of coupling interparticle diffusion to pore surface diffusion (Pan and Cocks, 1995; Zhang and Schneibel, 1995; Bouvard and McMeeking, 1996; Pan *et al.*, 1997) and linear elastic deformation to surface diffusion (Freund *et al.*, 1993; Suo and Wang, 1994; Wang and Suo, 1997; Xia *et al.*, 1997). Thouless (1993) has studied the effect of surface diffusion on the creep of sintered arrays of particles. Analogously, there are also models in the literature for stage II densification in which the dominant mechanism is one of those mentioned above, namely power-law creep (Cocks 1989; Duva and Crow, 1992; Sofronis and McMeeking, 1992), diffusional creep (Riedel *et al.*, 1994b) or interparticle diffusion and slip (Riedel *et al.*, 1994a). An overview of the analytical investigations into powder compaction is found in the work of Cocks (1994). In his paper, Cocks has laid out a methodology for formulating the constitutive laws for powder compacts. Furthermore, he has used appropriate kinematically and statically admissible fields to calculate bounds on macroscopic potentials that describe the densification process. Significantly, in this work, Cocks has taken into account the interaction between pairs of competing mechanisms in effecting the overall compaction of the particles.

Typically, in the work to date, one finds that not all the densifying mechanisms have been modeled in a synergistic framework. The interaction between the mechanisms could significantly affect the shapes of pores and the stress distribution along the interparticle contact areas, and hence macroscopic quantities like the relative density and the rate of densification. A systematic model that begins by considering the point contact between the particles and proceeds in time capturing and describing all the transient effects is still lacking.

There are also a number of assumptions that have been made in the past, the validity of which is an open question. A few of the models (McMeeking and Kuhn, 1992; Riedel *et al.*, 1994) have assumed the grains to be rigid and this implies that the normal velocity of separation between adjacent grains is a constant along their boundary. This simplifies the diffusion process on the interparticle contact areas and might give inaccurate results for the normal stresses and diffusional mass fluxes along the interparticle boundaries when other deformation processes are concurrently active. Treatment of the dihedral angle at the boundary of the interparticle contact area has also constituted a source of ambiguity. While it is certainly true that the well-known equilibrium expression for the dihedral angle in terms of the grain boundary and pore surface energies is valid for a static pore tip, the angle at the tip is not strictly equal to that dictated by the equilibrium relation when the interparticle area is growing. Still, it is not uncommon to find the strict enforcement of the dihedral angle at the tip during densification in several of the currently available models (Svoboda *et al.*, 1993; Bouvard and McMeeking, 1996; Pan and Cocks, 1995). Moreover, the equilibrium value of the angle is used to calculate the curvature at the tip of the pore. Thus, any untenable assumption regarding the angle could lead to a misleading description of the diffusion process at the tip. Lastly, even in the case when surface diffusion significantly affects

densification, one finds that the classical Laplace relationship connecting the curvature and surface energy of the pore to the normal stresses in the adjoining bulk material (Herring, 1951; Rice and Chuang, 1981; Freund *et al.*, 1993) is ignored. This relation is an important aspect of the underlying physics and its specification in the relevant initial boundary value problem cannot be omitted.

In the present work, the deformation of the powder aggregate is modeled by first determining the initial contact area due to elastic deformation that takes place instantaneously upon application of the external load. Subsequently, densification is considered to proceed under the combined action of linear elasticity and power-law creep in the bulk of the particles while diffusional mass transport occurs along the interparticle contact areas and pore surfaces. A finite element formulation is developed and implemented to solve the relevant initial boundary value problem under plane strain conditions. The pore surface energy appears in the formulation as it affects the pore surface diffusion and the magnitude of the stress acting normal to the pore surface. The surface energy of the interparticle contact area (grain boundary energy) is also accounted for in the formulation through the energy changes that occur when matter from the contact area is deposited onto the pore free surface. The proposed numerical scheme to solve the finite element equations is marched in time in order to capture the evolution of the pore shape and the closing of the porosity. The method provides an attractive means to keep track of the variation of the flux and curvature of the pore surface and the flux on the interparticle areas. The tip stress (i.e. the stress at the boundary of the interparticle area) and the corresponding curvature are calculated as part of the overall system equilibrium employed in the analysis and as a result, there is no need to make any restrictive assumptions with regard to their magnitude.

2. MATERIAL CONSTITUTIVE LAWS

The bulk of the particles is modeled as a homogeneous and isotropic material that deforms by linear elasticity and power-law creep. The total strain rate in the bulk is defined through the velocity as

$$\dot{\varepsilon}_{ij} = \left(v_{i,j} + v_{j,i}\right)/2, \tag{1}$$

where $(.)_{,j} = \partial(.)/\partial x_j$ and the superposed dot denotes differentiation with respect to time. The total strain is decomposed into elastic and creep strain components such that

$$\dot{\varepsilon}_{ij} = \dot{\varepsilon}^e_{ij} + \dot{\varepsilon}^c_{ij} . \tag{2}$$

The elasticity of the particle is characterized by the standard Hooke's law

$$\sigma_{ij} = C_{ijkl}\varepsilon^e_{ij} , \tag{3}$$

where C_{ijkl} are the components of the elastic modulus tensor, and the Einstein summation convention is implied over a repeated index. The creep strain rate $\dot{\varepsilon}^c_{ij}$ which obeys incompressibility is derived from

$$\dot{\varepsilon}^c_{ij} = \frac{\partial \phi^c}{\partial \sigma_{ij}} , \tag{4}$$

where

$$\phi^c = \frac{1}{1+n}\dot{\varepsilon}_0\sigma_0\left(\frac{\sigma_e}{\sigma_0}\right)^{1+n} \tag{5}$$

is the power-law creep potential, $\sigma_e = \sqrt{3s_{ij}s_{ij}/2}$ is the effective stress, $s_{ij} = \sigma_{ij} - (\sigma_{kk}/3)\delta_{ij}$ is the deviatoric stress, n is the creep exponent, $\dot{\varepsilon}_0$ and σ_0 are material constants, and δ_{ij} is the Kronecker delta. From Eqs. (4) and (5), one finds

$$\dot{\varepsilon}^c_{ij} = 3C\sigma_e^{n-1}s_{ij}/2\,, \tag{6}$$

where $C \equiv \dot{\varepsilon}_0/\sigma_0^n$ is the creep modulus.

Diffusion along the interparticle contact areas or the pore surface is motivated by chemical potential gradients such that

$$j_b = -\frac{D_b\delta_b}{kT}\frac{d\mu}{ds} \tag{7}$$

along the interparticle area, and

$$j_p = -\frac{D_p\delta_p}{kT}\frac{d\mu}{ds}, \tag{8}$$

along the pore surface. The parameter μ denotes the chemical potential of an atom, j_b and j_p are the volumetric fluxes per unit length along a direction s tangent to the interparticle area and pore surface respectively, D_b and D_p are the corresponding diffusion coefficients, δ_b and δ_p are the corresponding effective thicknesses through wich matter diffuses, k is Boltzmann's constant and T is the absolute temperature.

Following Herring (1951), one can write

$$\mu = -\sigma_n\Omega \tag{9}$$

along the interparticle area, and

$$\mu = -\gamma_p(k_1 + k_2)\Omega \tag{10}$$

along the pore surface, where σ_n is the stress normal to the contact area, k_1 and k_2 are the principal curvatures of the pore surface, and Ω is the atomic volume of the diffusing species. Combining Eqs. (7) and (9), and (8) and (10), yields respectively

$$j_b = \mathcal{D}_b\frac{d\sigma_n}{ds} \tag{11}$$

and

$$j_p = \mathcal{D}_p\frac{d[\gamma_p(k_1 + k_2)]}{ds}, \tag{12}$$

where now $\mathcal{D}_b = D_b\delta_b\Omega/kT$ and $\mathcal{D}_p = D_p\delta_p\Omega/kT$ are correspondingly interparticle and pore surface diffusivities having dimensions of volume divided by stress per unit time.

Matter conservation along the interparticle contact area requires

$$\frac{dj_b}{ds} + \dot{h} = 0\,, \tag{13}$$

where $\dot{h}$ is the normal velocity of interpenetration that would have resulted had the particles penetrated into one another under the action of the external loads. Denoting by

$\dot{g}$ the rate of change of the gap g (see Fig. 1a) between two points on the boundaries of particles I and II which are coming into contact with each other with corresponding velocities v_i^I and v_i^{II}, one can calculate the normal interpenetration velocity as

$$\dot{h} = \left(v_i^{II} - v_i^I\right) n_i + \dot{g}\,, \tag{14}$$

where n_i are the components of the unit normal to the contact area as shown in Fig. 1a. Notice that at any point along the contact area ($g = 0$, $\dot{g} = 0$), any change in the relative velocity $\left(v_i^{II} - v_i^I\right) n_i$ results directly in a change in the volumetric flux. Matter conservation for diffusion along the pore surface dictates that

$$\frac{dj_p}{ds} - v_n = 0\,, \tag{15}$$

where v_n is the velocity component normal to the pore surface with the unit normal vector pointing into the particle. A negative value of v_n implies that material is being deposited on the pore surface whereas a positive value implies erosion of the surface.

Considering the pore surface as a stretched membrane under the action of a constant surface tension and normal stresses σ_n from the adjoining bulk material, one can state the requirement for equilibrium at any arbitrary point by means of the standard Laplace equation (Gurtin and Murdoch, 1975; Rice and Chuang, 1981; Freund *et al.*, 1993)

$$\sigma_n = \gamma_p (k_1 + k_2). \tag{16}$$

The sign conventions for the curvature and the normal stress are shown in Fig. 1b. At the junction between the interparticle contact area and the pore surfaces, both volumetric flux and chemical potential are continuous. By Eqs. (10) and (11), chemical potential continuity requires that

$$(\sigma_n)_0 = \left[\gamma_p (k_1 + k_2)\right]_0\,, \tag{17}$$

where the subscript 0 is used to denote values at the junction.

3. THE UNIT CELL -- INITIAL BOUNDARY VALUE PROBLEM IN PLANE STRAIN

The problem of densification of a square array of cylinders under hydrostatic loading is considered (see Fig. 2). So the present analysis simulates hot isostatic pressing (HIPing) under plane strain deformation conditions. Pure HIPing was considered solely to reduce the amount of numerical complexities that would arise from interparticle slip if the applied macroscopic stress had a nonzero deviatoric component. It should be emphasized that the formulation developed in this work is equally valid for general loading states, though an appropriate unit cell has to be chosen to accommodate the applied stresses and appropriate modifications to the governing equations have to be made to account for interparticle slip (Needleman and Rice, 1980 and Casagranda and Sofronis, 1997). Due to the symmetry of the arrangement, the densification is studied by considering the deformation of just one quadrant of the cylinder as shown in Figs. 2 and 3. Clearly, this cell is only one of many that could have

been used. This particular choice has been made in view of the fact that the unit normals to the contact areas are known *a priori*. This offers a significant simplification with respect to the numerical evaluation of the contact areas and reduces the number of iterations and computation time considerably. As is evident from Fig. 3, there are two straight contact areas (line segments BC and DE) that develop upon loading, with the pore surface (arc CD) lying in between. Lastly, in view of the plane strain assumption, the only nonzero curvature is the in-plane one and it is denoted by k.

Extending the formulation of Needleman and Rice (1980) to include the effects of interface and pore surface energies, and pore surface diffusion, one can cast the governing equilibrium equations for the deformation of the cell in the following variational form

$$\int_{S_T} T_i \delta v_i ds = \int_A \sigma_{ij} \delta \dot{\varepsilon}_{ij} dA + \int_{S_b} \sigma_n \delta v_n ds + \int_{S_p} \sigma_n \delta v_n ds + \gamma_b \dot{a}_1 - \gamma_p (\delta v_{tip} \cos\phi)_C + \gamma_b \dot{a}_2 - \gamma_p (\delta v_{tip} \cos\phi)_D . \tag{18}$$

Here, T_i is the specified traction on the boundary S_T over which tractions are prescribed, σ_{ij} is the stress tensor within the bulk region A occupied by the particles (Fig. 3), δv_i is an arbitrary virtual variation of the velocity that vanishes on the part where velocities are prescribed, $\delta \dot{\varepsilon}_{ij}$ is the corresponding strain rate variation, σ_n is the normal stress either on the interparticle area S_b or the pore surface area S_p (Fig. 3), δv_n is the virtual variation of the normal velocity on S_b and S_p, s denotes arclength along the boundary BCDE measured from point B (Fig. 3), and ϕ is the dihedral angle at points C and D and is schematically shown in Fig. 1b. The parameters $\dot{a}_1$ and $\dot{a}_2$ are rates of change of the two contact areas and δv_{tip} is the velocity at the junctions measured positive if it causes an increase in the area of contact. The term on the left-hand side of the equation is the external virtual power delivered to the system and the terms on the right sum up to the total internal power. The integral evaluated on S_p represents the power expended in changing the pore surface area as it moves normal to itself during loading. The terms involving γ_b and γ_p represent the power expended/released as the densification proceeds and matter exchange occurs between interparticle boundaries and pore surface accompanied by corresponding changes in surface energy.

Starting with Eq. (11) and using the divergence theorem, one can state the principle of virtual power on the interparticle contact areas as

$$\int_{S_b} \sigma_n \delta v_n ds = \int_{S_b} \frac{1}{\mathcal{D}_b} j_b \delta j_b ds + (\sigma_n \delta j_b)_D - (\sigma_n \delta j_b)_C , \tag{19}$$

where δj_b and δv_n are respectively virtual flux and normal velocity fields that satisfy the zero flux condition at points B and D and are related by $d\delta j_b/ds + \delta v_n = 0$. Substituting Eqs. (19) and (16) into Eq. (18), one obtains the final variational statement for the densification process as follows:

$$\int_{S_T} T_i \delta v_i ds = \int_A \sigma_{ij} \delta \dot{\varepsilon}_{ij} dA + \int_{S_p} \gamma_p k \delta v_n ds + \int_{S_b} \frac{1}{\mathcal{D}_b} j_b \delta j_b ds + (\sigma_n \delta j_b)_D - (\sigma_n \delta j_b)_C$$
$$+\gamma_b \dot{a}_1 - \gamma_p (\delta v_{tip} \cos\phi)_C + \gamma_b \dot{a}_2 - \gamma_p (\delta v_{tip} \cos\phi)_D. \tag{20}$$

Equation (20) is solved for displacements by the finite element method. Using appropriate interpolation matrices for the relevant quantities, the variational statement is converted into a set of non-linear equations for the nodal velocities, or equivalently, the nodal displacement increments. There are two sources of non-linearity in the resulting equations: the power-law creep nature of the material, and the development and evolution of the interparticle contact areas. The contact areas, which are domains for the interparticle diffusion process, are not known beforehand and are determined as part of the solution. To this end, an iterative scheme has been proposed to systematically evaluate the contact areas as well as the creep strains occurring in the particles.

With regard to the contact areas, the strategy is to assume sizes for the contact areas that are in excess of the expected, and solve the boundary value problem at a given time t_{n+1} for displacements and stresses when the solution is known at time t_n. The solution is obtained by calculating increments to the known displacements at time t_n such that the governing Eq. (20) is satisfied at time t_{n+1}. Then, the stresses along the contact areas are checked for consistency, i.e., whether the stresses are compressive and nodes assumed to be diffusive are indeed in contact. If either of these conditions is not met, the assumed contact areas are reduced by a node and the procedure is repeated till the solution obtained is consistent.

In setting up the finite element equations for the displacement increments, the creep strain increment portion (cf. Eq. (2)) of the total strain increment associated with a displacement increment is unknown. As a result, the procedure for obtaining the solution for each set of assumed contact areas BC and DE (Fig. 3) is also iterative in nature (see Appendix A). For an assumed displacement increment, a creep strain increment is calculated pointwise as shown in Appendix C by the Newton iteration method ("local" iterative scheme). The finite element equations are then set up and solved for a new displacement increment also by the Newton iteration method ("global" iterative scheme). The creep strain rates are then corrected and these coupled "local" and "global" iterative schemes continue till convergent increments of displacement and creep strain are obtained, of course, for the assumed contact areas BC and DE. The creep strain rate and displacement increments at time t_n were used to initiate the process. Thus, since the solution to the initial boundary value problem involves also the simultaneous evaluation of the contact areas, a three-level iterative scheme has been devised to perform the task.

On the pore surface, except at the tip nodes at C and D (Fig. 3), the curvature is calculated at nodal positions i using the local position coordinates and those of the two neighboring nodes, $i-1$ and $i+1$. Thus (see Appendix D),

$$k_i = k_i(x_{i-1}, y_{i-1}, x_i, y_i, x_{i+1}, y_{i+1}), \tag{21}$$

where x_i and y_i are nodal coordinates. For the curvature at the tip, a quadratic extrapolation based on the curvatures at the three neighboring pore surface nodes is used. It ought to be emphasized that this way of calculating curvature is a point of departure from most of the previous work wherein, the tip curvature was calculated from the value of the dihedral angle, which was assumed to be strictly valid during the entire densification process.

The variational statement (20) enforces equilibrium in the bulk of the particles and ensures the satisfaction of the diffusion equation Eq. (11) on the interparticle boundaries BC and DE. However, it does not enforce the pore surface diffusion relation given by Eq. (12) or the local stress-curvature relation given by Eq. (16). These equations are strictly enforced as side constraints at time t_{n+1} during the iteration process. Since the numerically obtained solution to the stress, flux and curvature at time t_{n+1} is a function of the displacement increment, strict enforcement of Equations (12) and (16) leads to multi-point constraints along the boundary S_p. Moreover, the flux vanishes at points B and E owing to the square arrangement of particles. At B, the flux is zero by construction (see Appendix A) and at E, the zero flux boundary condition is enforced through a multi-point constraint that involves all the degrees of freedom (nodal velocities) on S_b and S_p.

4. DIMENSIONLESS GROUPS

A dimensional analysis over the geometric, material and loading parameters of the system leads to the following functional representation for the dependent variables:

$$\mathbf{a} = \mathbf{f}\left(\sigma_a/E, \nu, n, \psi_b, \psi_b, \chi_b, \chi_p, t/t_d\right), \tag{22}$$

where $\mathbf{a}$ is the non-dimensional version of a typical parameter such as displacement, strain-rate, stress etc., σ_a is the applied macroscopic stress on the aggregate (Fig. 3),

$$\psi_b = \frac{\gamma_b}{\sigma_a R}, \tag{23}$$

$$\psi_p = \frac{\gamma_p}{\sigma_a R}, \tag{24}$$

$$\chi_b = \frac{\mathcal{D}_b}{C\sigma_a^{n-1} R^3}, \tag{25}$$

$$\chi_p = \frac{\mathcal{D}_p \gamma_p}{C\sigma_a^{n} R^4}, \tag{26}$$

R is the particle radius, t_d is a time parameter that represents a characteristic time scale of the densification process, and isotropic elasticity was assumed for the particles with Young's modulus E and Poisson's ratio ν.

Clearly, ψ_b and ψ_p represent the strengths of the interface and pore surface tension in relation to the applied stress. The higher these values are, the larger is the energy required to be delivered by the applied load to change the respective areas of these surfaces. On the pore surface, a higher value of ψ_p implies higher normal

stresses in the adjoining bulk material. Next, it is shown that the dimensionless groups χ_b and χ_p characterize respectively the relative rates at which the interparticle and pore surface diffusion processes proceed in comparison to the power-law creep deformation of the bulk.

Groups χ_b and χ_p can be arrived at by considering the magnitudes of strain rates that are representative of the three densification processes, namely power-law creep deformation in the bulk, interparticle diffusion, and pore surface diffusion. A measure of the creep strain rate is readily expressed in terms of the creep constant and the applied stress through $\dot{\varepsilon}^c = C\sigma_a^n$. The diffusion processes can be thought of as resulting in strain rates, which in plane strain can be described by

$$\dot{\varepsilon}^b \approx \frac{\dot{A}_b}{A} \approx \frac{j_b}{R^2} = \frac{(\mathcal{D}_b \sigma_a / R)}{R^2} = \frac{\mathcal{D}_b \sigma_a}{R^3} \tag{27}$$

in the case of interparticle diffusion, and

$$\dot{\varepsilon}^p \approx \frac{\dot{A}_p}{A} \approx \frac{j_p}{R^2} = \frac{(\mathcal{D}_p \gamma_p / R^2)}{R^2} = \frac{\mathcal{D}_b \gamma_p}{R^4} \tag{28}$$

in the case of pore surface diffusion, where $\dot{A}_b$ and $\dot{A}_p$ are measures of rates at which the interparticle and pore surface diffusion processes transport mass per unit length in the out-of-plane direction and A is a measure of the area of the particle.

Characteristic time scales for each of the three rate mechanisms can be defined as the time required for the rate process to yield a strain equal to a reference strain, which is chosen as the elastic strain corresponding to the applied stress σ_a. Thus, the following characteristic times can be defined:

$$t_c = \frac{\varepsilon^e}{\dot{\varepsilon}^c} = \frac{\sigma_a / E}{C\sigma_a^n} = \frac{1}{EC\sigma_a^{n-1}} \tag{29}$$

for power-law creep deformation,

$$t_b = \frac{\varepsilon^e}{\dot{\varepsilon}_b} = \frac{R^3}{\mathcal{D}_b E} \tag{30}$$

for interparticle diffusion, and

$$t_p = \frac{\varepsilon^e}{\dot{\varepsilon}_p} = \frac{R^4 \sigma_a}{\mathcal{D}_p E \gamma_p} \tag{31}$$

for pore surface diffusion. Therefore, by means of Eqs. (27), (29) and (30), definition (25) is rewritten as

$$\chi_b = \frac{\dot{\varepsilon}_b}{\dot{\varepsilon}_c} = \frac{t_c}{t_b} = \frac{\mathcal{D}_b}{C\sigma_a^{n-1} R^3}. \tag{32}$$

Similarly, by means of Eqs. (28), (29) and (31), definition (26) is rewritten as

$$\chi_p = \frac{\dot{\varepsilon}_p}{\dot{\varepsilon}_c} = \frac{t_c}{t_p} = \frac{\mathcal{D}_p \gamma_p}{C\sigma_a^n R^4}. \tag{33}$$

It is obvious from Eqs. (32) and (33) that, for instance, if $\chi_b = 10$ and $\chi_p = 100$, one can infer that the interparticle and pore surface diffusion processes are respectively one and

two orders of magnitude faster than the power-law creep process in the bulk of the particles. Since the speed of the densification process is controlled by the smallest time constant, $t_d = \min(t_c, t_b, t_p)$ in Eq. (22).

5. NUMERICAL RESULTS

A notable feature of the formulation is that if the interparticle diffusion coefficient is assumed to have a very small value, and the free surface diffusion coefficient is set equal to zero, and any surface energy effects are neglected, it is equivalent to a penalty method treatment of the initial elastic contact problem. This feature was employed to calculate the elastic solution at time $t = 0$, which serves as the starting point for the subsequent time-dependent deformation of the unit cell. The solution was obtained for successive time steps by the procedure outlined in Section 3 and macroscopic quantities such as density and densification rates were calculated. The undeformed particle radius was $R = 1$ and this corresponds to an initial area fraction of particles of 0.785. Eight-noded isoparametric elements were used with a 2×2 rule for integration of stiffness matrices. The incompressibility of the creep deformation was enforced by the method of Nagtegaal, Parks and Rice (1974). The mesh used in the calculation has 920 elements and 2481 nodes, out of which 321 were sequentially numbered and placed along the arc BCDE to discretize the contact areas and the pore surface. The elasticity of the particles was assumed to be isotropic, and unless stated otherwise, the finite element results were obtained for $\chi_b = 10, \chi_p = 100,$ $\psi_p = \psi_b = 0.1, E/\sigma_a = 100, \nu = 0.33$, and creep exponent equal to 5. The applied macroscopic stress state was $\Sigma_{xx} = \Sigma_{yy} = -\sigma_a$ as shown in Fig. 3. With this choice of data, the smallest time constant is that for pore surface diffusion and hence $t_d = t_p$ (see Eq. (31)). The initial marching time step was $\Delta t = 10^{-6} t_p$, and as the powder aggregate relaxed and densified, the magnitude of the time step was increased. Calculations were carried out till the total elapsed time was equal to $t_p/2$. At this stage, nodal displacements were observed to be quite large and the present small-strain scheme with no nodal updating was deemed to be inadequate and hence no further computations were carried out. If t is the total elapsed time, then one can conclude from Eq. (29) that

$$\frac{\varepsilon^e}{\varepsilon^c} = \frac{t_c}{t} = \frac{\chi_p t_p}{t} \tag{34}$$

Since the largest value of t/t_p is 0.5 and $\chi_p = 100$, it is clear that during the entire range of deformation considered, the magnitude of the creep strains is small when compared to the elastic strains.

Figure 4 shows the flux profiles on the interparticle contacts and pore surface as a function of the arc length s at various values of the normalized time t/t_d. Note that $s = 0$ at point B and $s = s_{max}$ at point E (Fig. 3). The flux is normalized by a reference value $j_{ref} = \mathcal{D}_b \sigma_a / s_{max}$ and the stress by the magnitude of the applied stress σ_a. Peaks

in the magnitude of the volumetric flux coincide with the location of the boundaries of the interparticle areas (that is, points C and D), and the midpoint of the pore is a point of reflection for the flux profile. The anti-symmetry of the flux profiles about $s = s_{max}/2$ derives from the hydrostatic compaction feature, that is, equal amounts of mass diffuse out of the two contact areas BC and DE toward the pore surface. The flux profiles flatten out as time elapses and this is again in accordance with diffusion-induced stress and pore curvature relaxation whereby the gradients in stress and curvature reduce with time, thus resulting in less amounts of volumetric diffusion.

A typical normal stress σ_n/σ_a profile is shown in Fig. 5 for $0 \le s \le s_{max}$ along with the corresponding curve for flux at time $0.025t_d$. The normal stress becomes less compressive as one approaches the tips (points C and D in Fig. 4) and this translates to monotonically increasing values of volume flux. The tips are extremum points for the normal stress gradient and this is reflected in the maximum magnitude of the volume flux. As one moves past the tips and toward the pore surface, the normal stress variations become significantly less, but the higher value of pore surface diffusion parameter still leads to comparable flux magnitudes. The stress variation is symmetric with respect to the center of the pore surface and this agrees with the anti-symmetric nature of the flux profile. A snapshot of the flux and curvature variations on the pore surface at time $t = 0.025t_d$ is shown in Fig. 6. This plot illuminates the characteristics of surface diffusion over the pore. As one would expect from Eq. (12), the flux is negative when the curvature decreases, positive when it increases, and zero at maxima or minima. Figure 6 also indicates that the maximum absolute value of the non-dimensionalized curvature kR is less than 2. Therefore, for $\psi_p = 0.1$, Eq. (16) phrased in the form $\sigma_n/\sigma_a = kR\psi_p$, yields values for the non-dimensionalized stress σ_n/σ_a that are less than -0.2. This result is in excellent agreement with the normal stress levels over the pore surface shown in Fig. 5.

In Fig. 7, the normalized curvature kR of the pore surface is shown plotted against normalized arclength s/s_{max} at various instants of time. In accordance with the curvature sign convention, the curvature is negative throughout since the pore is convex. The expected symmetric variation about the mid-point is observed. As deformation proceeds, the entire curvature profile shifts upwards, i.e., the pore deforms so that its curvature gradients are neutralized and it becomes less curved.

Figure 8 shows the outline of the unit cell at different stages of deformation. One can readily observe the systematic increase in the sizes of the interparticle contact areas as well as the pattern of mass distribution. While the value of the surface diffusion parameter controls the pattern of mass distribution, thickening of the pore surface occurs due to deposition of mass moving out of the contact areas. For $\chi_p = 100$, while there seems to be a reasonably even distribution overall, more mass is deposited in the regions near the tip of the pore as compared to the interior.

In order to investigate the magnitude of the normal tip stress σ_0 (cf. Eq. (17)), additional calculations were carried out for $\chi_p = 10^4$, while the values of the other

parameters were held unchanged. Due to the nature of the loading, the stresses at the two tips are equal to each other. Figure 9 shows the variation of the tip stress plotted as a function of relative density. The deformation of the unit cell immediately following the initial elastic contact was characterized by sharp gradients in the stresses and rapid rates of increase in the contact sizes. As a result, the numerical scheme employed in this study was unable to capture the magnitude of the tip stresses with the desired accuracy. As mentioned in Appendix A, the scheme for calculation of the tip stress is an approximate one and this may be the reason for the lack of accuracy in the early stages. However, it should be emphasized that the solution for the displacement was always accurate, even during the early stages of deformation. The local tip stress values stabilized after additional densification and Fig. 10 shows the variation after the initial transients. It is seen that throughout the densification process, the stress at the tip is compressive. The initial, instantaneous elastic deformation leads to negligibly small compression at the beginning, but as soon as the diffusion processes set in, a dramatic drop in the stress occurs. Subsequently, as time elapses, there is a decrease in the magnitude of the tip stresses and this trend is milder in the case of $\chi_p = 10^4$ while the $\chi_p = 10^2$ case is characterized by a more pronounced variation. The figures also show the corresponding profiles of $(\gamma_p k)_0$ whose data points are indistinguishable from those of the tip stress, in accordance with Eq. (17).

Comparison with other models

The complete solution to the initial boundary value problem for the unit cell facilitates the calculation of the relative density D of the powder compact by determining the area fraction occupied by the particles. The densification rate $\dot{D}$ is then computed through the change ΔD occurring during the time increment Δt. Expressions for $\dot{D}$ are available in the literature from models based on different principal densifying mechanisms acting alone.

McMeeking and Kuhn (1992) considered the densification of an initially random close-packed aggregate of spherical particles deforming primarily by interparticle diffusion. They report the densification rate to be

$$\dot{D} = \frac{36(1-D_0)^2}{D(D-D_0)^2}\left(\frac{D}{D_0}\right)^{\frac{2}{3}} \frac{\mathcal{D}_b p}{R^3}, \tag{35}$$

where D_0 is the initial relative density which for random close-packing is 0.64 and p is the applied pressure. The numerical results of the present model are compared with those of Eq. (35) at the same macroscopic pressure prevailing during the densification process. This macroscopic pressure is essentially elastic, in view of the negligible creep response of the cell, and therefore it is taken to be $p = 2(1+\nu)\sigma_a/3$ under plane strain. Then, recalling definition (25) of χ_b, one can recast Eq. (35) into

$$\dot{D} = 24(1+\nu)\frac{(1-D_0)^2}{D(D-D_0)^2}\left(\frac{D}{D_0}\right)^{\frac{2}{3}}\chi_b C\sigma_a^n . \tag{36}$$

A slightly different result was obtained by Helle *et al.* (1985) for densification under pure interparticle diffusion. Making similar substitutions, one can rewrite their formula for the densification rate as

$$\dot{D} = \frac{86}{3}(1+\nu)\frac{(1-D_0)^2}{(D-D_0)^2}\chi_b C\sigma_a^n . \tag{37}$$

For the case of compaction by power-law creep deformation alone, Kuhn and McMeeking (1992) calculate that the densification rate for purely hydrostatic compression is given by

$$\dot{D} = \frac{27\pi}{16\sqrt{3}}\left[\frac{2(1+\nu)}{9}\right]^n D\left(\frac{D-D_0}{1-D_0}\right)^{\frac{1}{2}}\left[\frac{(1-D_0)}{D^2(D-D_0)}\right]^n C\sigma_a^n . \tag{38}$$

Under the same conditions, Helle *et al.* (1985) calculate the densification rate to be

$$\dot{D} = \frac{5.3}{\sqrt{3}}\left[\frac{2(1+\nu)}{9}\right]^n (D^2 D_0)^{\frac{1}{3}}\left(\frac{D-D_0}{1-D_0}\right)^{\frac{1}{2}}\left[\frac{(1-D_0)}{D^2(D-D_0)}\right]^n C\sigma_a^n . \tag{39}$$

Figure 10 shows the comparison of the densification rate obtained using the finite element results of the present model at $\chi_b = 10$ and two different values of χ_p, namely 10^2 and 10^4, with the corresponding results that Eqs. (36)-(39) yield. The interparticle diffusion models of Eqs. (36) and (37) agree very well with each other and so do the two power-law creep models of Eqs. (38) and (39). The densification rates furnished by the interparticle diffusion models are several orders of magnitude greater than those from the power-law creep models, as expected, since densification by interparticle diffusion is much faster than by power-law creep in the bulk. The present investigation predicts initial densification rates an order of magnitude higher than those of the grain boundary diffusion models, but these decrease rapidly and fall between the values calculated from the models employing interparticle diffusion alone and those using power-law creep alone. Obviously, the very high initial densification rates during the early stages (at low relative density) result from the rapid diffusion processes associated with the initial, severe elastic stress gradients. As densification proceeds and the diffusional relaxation mechanisms alleviate and neutralize these gradients (see Fig. 4), the densification rates drop to lower levels. The parameter χ_p seems to have a moderate but definite effect on the densification rate. It should be borne in mind that the diffusional creep models of Eqs. (36) and (37) are predicated on pore surface diffusion that is very fast in comparison to the interparticle diffusion. Therefore, the finite element results of Fig. 10 denoted by the lower curve ($\chi_p = 10^4$) should be considered in comparing the models.

Comparison with experimental data

Casagranda *et al.* (1996) performed a series of constant strain rate densification experiments using cylindrical compact specimens of porous alumina specimens under uniaxial compression over a wide variety of temperatures. The imposed strain rates varied between 3×10^{-6} and $3\times10^{-5}/s$ and the temperatures between 1050°C and 1200°C. Analyzing their results, Casagranda *et al.* observed that when the densification rates were cast in the non-dimensional form

$$\alpha(t) = \frac{\dot{E}kT\mu d^2}{D_b\delta_b b^2}\left(\frac{1}{\Sigma(t)}\right)^2, \tag{40}$$

where $\dot{E}$ is the applied compressive strain rate, Σ the measured macroscopic stress on the specimen, μ the shear modulus, d the particle diameter, and b the Burgers vector, the calculated values of α for all the experiments ranged from 1 to 10, and collapsed onto a narrow band that decreases in magnitude with increasing relative density.

Model calculations were carried out using data for alumina (Tables 1 and 2) at 1100° C for three of the stress levels Casagranda *et al.* measured in the their experiments, namely 100 MPa, 110 MPa and 125 MPa. The calculated macroscopic dilatation rate $\dot{E}_{kk} = -2\dot{\varepsilon}_a$ (Fig. 3) was then used to derive a one-dimensional macroscopic compressive strain rate $\dot{E}$ such that $3\dot{E} = -\dot{E}_{kk}$. Similarly, the macroscopic pressure $p = 2(1+\nu)\sigma_a/3$ was set equal to the pressure $\Sigma/3$ in simple uniaxial compaction under compressive stress Σ. Next, Eq. (40) was used to calculate the values of the non-dimensionalized strain rate α associated with the finite element calculation results. These values are illustrated in Fig. 11. At a given stress Σ, the strain rate $\dot{E}$ decreases with time and since $\alpha(t)$ is proportional to $\dot{E}$ (Eq. (40)), so does α as shown in the figure. The values of α computed from strain rates obtained from the model calculations are shown by hollow symbols connected by dotted lines while the values of α corresponding to the experimental strain rates, calculated using Eq. (40), are shown by solid symbols connected by solid lines. Due to the limitations imposed by the small-strain assumption employed in the current scheme, calculations were performed over a small range of densification. The lowest strain rates corresponding to the finite element data shown in Fig. 11 are of the order of $10^{-4}/s$ which is still 1-2 orders of magnitude greater than those used in the experiments of Casagranda *et al.* Thus, the corresponding lowest values of α obtained from the present numerical calculations are of the order of around 500 which is notably also 1-2 orders of magnitude greater than the range of 1-10 obtained by Casagranda *et al.*. Keeping this observation in mind and looking at the monotonically decreasing trend exhibited by α, one may reasonably expect the values of α one could obtain numerically for the strain rates employed in the experiments of Casagranda *et al.* to agree well with those obtained experimentally.

Using cylindrical specimens, Kim (1997) carried out sinter-forging experiments on Ti-48Al powder with an average grain size of 10 microns. Compaction took place

under uniaxial compressive stress at values varying from $200-500\,\mathrm{MPa}$ and held constant during densification at a temperature of $625^{\circ}\mathrm{C}$. With the use of material data for γ-TiAl (Tables 3 and 4) model calculations were performed under macroscopic stresses of $\sigma_a = 300$, 400 and 500 MPa. As with the definition of the macroscopic strain rate $\dot{E}$, a uniaxial compressive macroscopic strain E was defined through $E = 2(E^{el} + \int_0^t \dot{\varepsilon}_a dt')/3$, where E^{el} is the strain in the unit cell at the end of the initial elastic contact. Figure 12 shows this numerically calculated strain E as a function of time. As observed by Kim, the strains increase monotonically with time, and not surprisingly, higher stresses lead to higher strains. Experiments were performed by Kim for time durations as long as 5500 seconds, whereas due to the limitations of the current numerical scheme mentioned in the preceding paragraph, computations only spanned much shorter periods of time. In spite of this, quantitative agreement with Kim's experiments seems to be quite good. For instance, under a stress of 500 MPa, a strain of 0.8% was calculated at $t = 40s$, while the corresponding Fig. 44 of Kim (1997) shows a strain of around 1%.

6 DISCUSSION

From Fig. 4 it is seen that at time $t = 0.005t_d$, the flux reverses sign at two pairs of symmetrically placed points on the pore surface and by Eq. (12), the curvature exhibits stationary values at these points as shown in Fig. 6. However at time $t = 0.03t_d$, there is only one pair of points at which this happens and for the times $t = 0.125t_d$ and $t = 0.300t_d$, the flux decreases monotonically from tip to tip. Thus, the surface diffusion process is very effective in neutralizing the local curvature gradients and setting up a linearly varying flux pattern.

The calculations shown in Fig. 5 indicate that the interparticle boundaries and the pore surface are all in a state of compression. The compressive stress on the interparticle areas decreases as one moves towards the tip, thus setting up stress gradients that force the mass out through the boundaries and onto the pore surface. The chemical potential is higher on the pore surface at regions of higher convexity and atoms there tend to move toward regions of less convexity or concavity. Interparticle diffusion is the primary source of rearrangement of matter and hence, χ_b has a central role to play in determining the magnitude of mass flux at the tip of the interparticle contacts. However, it is also essential that the pore surface be capable of efficiently absorbing the mass emanating from the contact areas and therefore, the rate of mass transfer also depends directly on the magnitude of the surface diffusion parameter χ_p. Consequently, so does the pattern of redistribution of the flux coming onto the pore from the interparticle areas. Slow surface diffusion leads to an accumulation of mass near the tips and this in turn retards the flux at the tip. As a result, there is a decrease in the densification rate. On the other hand, fast surface diffusion enables the pore

surface to absorb all the mass flowing out of the contact areas and this leads to higher densification rates.

The above argument is clearly supported by Fig. 10 wherein the densification rates obtained for the two different values of χ_p are noticeably different. One can also see from the figure that modeling the processes accurately is very crucial in determining the macroscopic behavior. Depending on which mechanism is assumed to dominate, rates of densification that are several orders of magnitude apart can be obtained. The results shown in Fig. 10 also suggest that densification that occurs solely by grain boundary diffusion or power-law creep should be treated as a limiting case. At the outset, the densification rates are closer to those predicted by models of densification dominated by grain boundary diffusion, but as time elapses and diffusion slows down due to stress and curvature gradient relaxation, the bulk deformation in the particles tends to affect the process. It seems that at very high relative densities, the densification rates tend to approach those predicted by the power-law creep models.

As shown in Fig. 11, the present finite element model predicts dimensionless densification rates for Al_2O_3 for three different stress levels that are compatible with the experimental results of Casagranda *et al.* (1996). Also, there is good agreement between the predicted and experimentally obtained strain in the case of TiAl compacts (Kim, 1997). However, it is important to note that both sets of experiments were uniaxial compression tests while the present model simulates plane strain densification. Therefore, the comparisons that have been made using the derived one-dimensional stress and strains as explained in Section 5 involve a certain amount of approximation. Casagranda *et al.* concluded that powder compaction in their experiments was controlled by the interparticle diffusion mechanism. This is in agreement with our numerical results that indicate a synergistic dominance of interparticle and pore surface diffusion, at least during the early stages of deformation.

An important result of the present finite element calculations regards the prediction of the evolving shape of the pore surface during densification (see Fig. 8). Clearly, the curvature of the pore remains negative (convex) during the early stages of the densification. Thus, the phenomenon of curvature sign reversal along the pore surface, as postulated and employed in the analysis of some two-particle densification models, was not observed in the calculations. However, simulations spanning longer times are required in order to assess whether pore convexity continues to be maintained during the entire stage I densification process or, if that is not the case, to identify the time at which the pore surface begins to develop concave segments as the process advances toward stage II.

7 CLOSURE

Densification of a powder aggregate is a complex physical phenomenon involving multiple mechanisms characterized by a large number of material and geometric parameters. In the present study, important dimensionless groups have been

identified and this leads to a dramatic reduction in the number of the case calculations required to analyze the process.

A finite element methodology has been developed to study the densification process of a particle aggregate based on the interaction between the mechanisms acting at the microscale. In view of the complexity of the governing equations, one may consider the devised numerical techniques as fairly robust in predicting the values of both microscopic and macroscopic parameters when pore and particle shape changes are small. For predictions pertaining to times closer to the end of stage I densification, the present model needs to be modified to account for geometric nonlinearities.

The finite element calculations show that the overall densification rate is sensitive to the strength of the pore surface diffusion. Available models based on a single operating mechanism have been shown to either overestimate (diffusional creep) or underestimate (power-law creep) the densification rates due to the neglect of the coupling between the densification mechanisms. Lastly, during the early stages of the densification process, the pore surface curvature maintains the same sign all along the pore surface.

8 ACKNOWLEDGEMENT

This work was supported by the Department of Energy under grant DEFGO2-91ER45439. The authors would like to thank Professor R. S. Averback for many helpful discussions on the physics of the densification process.

TABLE 1: Material properties for Al_2O_3 (Helle *et al.*, 1985; Ashby, 1990).

Surface energy $= 0.90\ \mathrm{J/m^2}$

Atomic Volume $\Omega = 1.42\times10^{-29}\ \mathrm{m^3}$

Melting point $T_m = 2320\mathrm{K}$

Burgers vector $b = 4.76\times10^{-10}\ \mathrm{m}$

Young's modulus E = 395 GPa at room temperature

Shear modulus

$$\mu = \mu_0\left[1+\frac{(T-300)}{T_m}\left(\frac{T_m d\mu}{\mu_0 dT}\right)\right],\quad \mu_0 = 155\ \mathrm{GPa\ at\ 300K}$$

$$\left(\frac{T_m d\mu}{\mu_0 dT}\right) = -0.35$$

Power-law creep: $\dot{\varepsilon} = D_c\left(\frac{\sigma}{\sigma_{ref}}\right)^n,\quad D_c = 10^{-6}\exp[\frac{-Q_c}{RT_m}(\frac{T_m}{T}-2)]$

Activation energy $Q_c = 477.0\mathrm{kJ/mol}$

Power-law creep exponent $n = 3$

Reference Stress $\sigma_{ref} = 1250\ \mathrm{MPa}$

Volume diffusion: $D_v = D_{0v}\exp(-\frac{Q_v}{RT})$

Activation energy $Q_v = 477.0\ \mathrm{kJ/mol}$

Pre-exponential $D_{0v} = 1.2\times10^{-6}\ \mathrm{m^2/s}$

Grain boundary diffusion: $D_b\delta_{ib} = D_{0b}\delta_{0b}\exp(-\frac{Q_b}{RT})$

Activation energy $Q_b = 419.0\ \mathrm{kJ/mol}$

Pre-exponential $D_{0b}\delta_0 = 8.6\times10^{-10}\ \mathrm{m^3/s}$

Surface diffusion: $D_p\delta_p = D_{0p}\delta_{0p}\exp(-\frac{Q_p}{RT})$

Activation energy $Q_p = 500.0\ \mathrm{kJ/mol}$

Pre-exponential $D_{0p}\delta_{0p} = 8.6\times10^{-6}\ \mathrm{m^3/s}$

TABLE 2: Values of the dimensionless groups for alumina at 1100 ^{0}C at different stresses.

Σ (MPa)	χ_b	χ_p	$\psi_b = \psi_p$	E/σ_a	$t_d (= t_p)$ (s)
100	43	81	0.228	8381	21.7
110	35	61	0.208	7619	23.9
125	27	42	0.183	6704	27.1

TABLE 3: Material properties for γ -TiAl (Ashby, 1990).

Surface energy $= 1.76\ \mathrm{J/m^2}$

Atomic Volume $\Omega = 3.11\times10^{-29}\ \mathrm{m^3}$

Melting point $T_m = 1730$ K

Young's modulus E = 168 GPa at room temperature

Power-law creep: $\dot{\varepsilon} = D_c\left(\frac{\sigma}{\sigma_{ref}}\right)^n$, $D_c = 10^{-6}\exp[\frac{-Q_c}{RT_m}(\frac{T_m}{T}-2)]$

Activation energy $Q_c = 320.0\ \mathrm{kJ/mol}$

Power-law creep exponent $n = 3$

Reference Stress $\sigma_{ref} = 1800$ MPa

Grain boundary diffusion: $D_b\delta_{ib} = D_{0b}\delta_{0b}\exp(-\frac{Q_b}{RT})$

Activation energy $Q_b = 180.0\ \mathrm{kJ/mol}$

Pre-exponential $D_{0b}\delta_0 = 7.6\times10^{-13}\ \mathrm{m^3/s}$

Surface diffusion: $D_p\delta_p = D_{0p}\delta_{0p}\exp(-\frac{Q_p}{RT})$

Activation energy $Q_p = 150.0\ \mathrm{kJ/mol}$

Pre-exponential $D_{0p}\delta_{0p} = 7.6\times10^{-10}\ \mathrm{m^3/s}$

TABLE 4: Values of the dimensionless groups for $\gamma - TiAl$ at 625^0C at different stresses.

Σ (MPa)	χ_b	χ_p	$\psi_b = \psi_p$	E/σ_a	$t_d(=t_p)$ (s)
300	40	6485	0.0029	1269	78.1
400	22	2735	0.0022	952	104.1
500	14	1400	0.0018	761	130.1

REFERENCES

Akisanya, A. R. and Cocks, A. C. F., 1995. Stage I compaction of cylindrical particles under non-hydrostatic loading. *J. Mech. Phys. Solids* 43 (4), 605-636.

Akisanya, A. R., Cocks, A. C. F. and Fleck, N. A., 1994. Hydrostatic compaction of cylindrical particles. *J. Mech. Phys. Solids* 42 (7), 1067-1085.

Arzt, E., 1982. The influence of an increasing particle coordination on the densification of spherical powders. *Acta Metal.* 30 (10), 1883-1890.

Arzt, E., Ashby, M. F. and Easterling, K. E., 1983. Practical applications of hot-isostatic pressing diagrams: Four case studies. *Metal. Trans.* 14A (2), 211-221.

Ashby, M. F., 1969. On interface-reaction control of Nabarro-Herring creep and sintering. *Scr. Metal.* 3 (11), 837-842.

Ashby, M. F., 1974. A first report on sintering diagrams. *Acta Metal.* 22 (3), 275-289.

Ashby, M. F., 1990. HIP 6.0 User Manual.

Bouvard, D., 1993. Modeling the densification of powder composites by power law creep. *Acta Metal. Mater.* 41 (5), 1413-1420.

Bouvard, D. and McMeeking, R. M., 1996. The deformation of interparticle necks by diffusion controlled creep. *J. Am. Cer. Soc.* 79 (3), 666-672.

Burton, B., 1972. Interface reaction controlled diffusional creep: a consideration of grain boundary dislocation climb sources. *Mat. Sci. Engg.* 10 (1), 9-14.

Casagranda, A., Xu, J., Evans, A. G. and McMeeking, R. M., 1996. Pressure consolidation of fiber-reinforced oxide matrix composites: experiments and simulations. *J. Am. Ceram. Soc.* 79 (5), 1265-1272.

Casagranda, A., and Sofronis, P., 1997. Numerical observations of scaling laws in the consolidation of powder compacts. *Acta Mater.* 45 (11), 4835-4845.

Chuang, T.-J., Kagawa, K. I., Rice, J. R. and Sills, L. B., 1979. Non-equilibrium models for diffusive cavitation of grain interfaces. *Acta Metal.* 27 (3), 265-284.

Choi, B. W., Deng, Y. G., McCullough, C., Paden, B. and Mehrabian R., Densification of rapidly solidified titanium aluminide powders --- I. Comparison of experiments to HIPing models. *Acta Metal.* 38 (11), 2225-2243.

Cocks, A. C. F., 1989. Inelastic deformation of porous materials. *J. Mech. Phys. Solids* 37 (6) 693-715.

Cocks, A. C. F., 1992. Interface reaction controlled creep. *Mech. Mater.* 13 (2), 165-174.

Cocks, A. C. F., 1993. The structure of constitutive laws for the sintering of fine-grained materials. *Acta Metal. Mater.* 42 (7) 2191-2210.

Cocks, A. C. F. and Du, Z.-Z., 1993. Pressureless sintering and hiping of inhomogeneous ceramic compacts. *Acta Metal. Mater.* 41 (7), 2113-2126.

Duva, J. and Crow, P. D., 1992. The densification of powders by power law creep during hot isostatic pressing. *Acta Metal. Mater.* 40 (1), 31-35.

Fishcmeister, H. F. and Arzt, E., 1983. Densification of powders by particle deformation. *Pow. Metal.* 26 (2), 82-88.

Fleck, N. A., 1995. On the cold compaction of powders. *J. Mech. Phys. Solids,* 43 (9) 1409-1431.

Fleck, N. A., Kuhn, L. T. and McMeeking, R. M., 1992. Yielding of metal powder bonded by isolated contacts. *J. Mech. Phys. Solids,* 40 (5), 1139-1162.

Freund, L. B., Beltz, G. E., and Jonsdottir, F., Continuum modeling of stress-driven surface diffusion in strained elastic materials. *Mat. Res. Soc. Symp. Proc.* 308, 383-394.

Gurtin, M. E. andn Murdoch, A. I., 1975. A continuum theory of elastic material surfaces. *Arch. Rat. Mech. Anal.* 57 (4), 291-323.

Helle, A. S., Easterling, K. E. and Ashby, M. F., 1985. Hot-isostatic pressing diagrams: New developments. *Acta Metal.* 33 (12) 2163-2174.

Herring, C., 1951. Surface tension as a motivation for sintering. In: The Physics of Powder Metallurgy - A symposium held at Bayside, L. I., New York, August 24-26, 1949, pp 143-179.

Kim, L. S., 1997. Synthesis, consolidation and mechanical testing of nanophase metals, Ph.D. Thesis, University of Illinois.

Kuhn, L. T. and McMeeking, R. M., 1992. Power law creep of powder bonded by isolated contacts. *Intl. J. Mech. Sci.* 34 (7), 563-573.

McMeeking, R. M. and Kuhn, L. T., 1992. A diffusional creep law for powder compacts. *Acta Metal. Mater.* 40 (5), 961-969.

Nagtegaal, J. C., Parks, D. M., and Rice, J. R., On numerically accurate finite element solutions in the fully plastic range. *Comp. Meth. Appl. Mech. Engg.* 4 (2), 153-177.

Needleman, A. and Rice, J. R., 1980. Plastic creep flow effects in the diffusive cavitation of grain boundaries. *Acta Metal.* 28 (10), 1315-1332.

Pan, J. and Cocks, A. C. F., 1995. A numerical technique for the analysis of coupled surface and grain-boundary diffusion. *Acta Metal. Mater.* 43 (4), 1395-1406.

Pan, J., Cocks, A. C. F. and Kucherenko, S., 1997. Finite element formulation of coupled grain-boundary and surface diffusion with grain-boundary migration. *Proc. Roy. Soc. Lond.* A 453 (1965) 2161-2184.

Rice, J. R. and Chuang, T.-J., 1981. Energy variations in diffusive cavity growth. *J. Am. Cer. Soc.* 64 (1), 46-53.

Riedel, H., Kozak, V. and Svoboda, J., 1994a. Densification and creep in the final stage of sintering. *Acta Metal. Mater.* 42 (9) 3093-3103.

Riedel, H., Zipse, H. and Svoboda, J., 1994b. Equilibrium pore surfaces, sintering stresses and constitutive equations for the intermediate and late stages of sintering – II. Diffusional densification and creep. *Acta Metal. Mater.* 42 (2) 445-452.

Schafrik, R. E., 1977. Dynamic elastic moduli of the Titanium Aluminides. *Metal. Trans.* 8A (6), 1003-1006.

Sofronis, P. and McMeeking, R. M., 1992. Creep of power-law material containing spherical voids. *J. Appl. Mech.* 59 (2), S88-S95.

Suo, Z. and Wang, W., 1994. Diffusive void bifurcation in stressed solid. *J. Appl. Phys.* 76 (6), 3410-3421.

Svoboda, J. and Riedel, H., 1995. New solutions describing the formation of interparticle necks in solid-state sintering. *Acta Metal. Mater.* 43(1), 1-10.

Svoboda, J., Riedel, H. and Zipse, H., 1994. Equilibrium pore surfaces, sintering stresses and constitutive equations for the intermediate and late stages of sintering – I. Computation of equilibrium surfaces. *Acta Metal. Mater.* 42(2), 435-443.

Swinkels, F. B. and Ashby, M. F., 1981. A second report on sintering diagrams. *Acta Metal.* 29 (2), 259-281.

Thouless, M. D., 1993. Effect of surface diffusion on the creep of thin films and sintered arrays of particles. *Acta Metal. Mater.* 41 (4), 1057-1064.

Wang, W. and Suo, Z., 1997. Shape change of a pore in a stressed solid via surface diffusion motivated by surface and elastic energy variation. *J. Mech. Phys. Solids* 45 (5), 709-729.

Xia, L., Bower, A. F., Suo, Z. and Shih, C. F., 1997. A finite element analysis of the motion and evolution of voids due to strain and electromigration induced surface diffusion. *J. Mech. Phys. Solids* 45 (9), 1473-1493.

Zhang, W. and Schneibel, J. H., 1995. The sintering of two particles by surface and grain-boundary diffusion – a two-dimensional numerical study. *Acta Metal. Mater.* 43 (12), 4377-4386.

APPENDIX A: FINITE ELEMENT FORMULATION AND SOLUTION OF THE INITIAL BOUNDARY VALUE PROBLEM

A1. Formulation

Under plane strain conditions, the interparticle contact areas are assumed to be the two plane segments BC and DE of Fig. 3. Arclength s is measured starting from point B and increases toward point E. As time elapses, the contact areas develop and

typically different nodes define the end of the contact areas at different times. These nodes are not known at the start of the calculation and have to be determined as part of the solution. One contact segment is defined by the line $y = -R$ and the other by $x = R$. The normal n is defined on the contact areas as positive when it points inwards as shown in Fig. 1a. A non-negative scalar gap function $g(s)$ at any point of the particle surface is defined to be its normal distance from the contact plane. If a node is already in contact, the value of the gap function is set to 0. From the initial position of the nodes and their subsequent deformation, $g(s)$ is easily calculated since the normal and the position of the contact surface do not change with time. Once the gap function is established, for $v^{II} = 0$ and $v^{I} = v$, Eq. (14) yields

$$\dot{h} = \dot{v}_n + \dot{g} = v_\alpha n_\alpha + \dot{g} . \tag{A1}$$

Here $\dot{g} = g/\Delta t$ and measures the rate at which a node that was separated by an amount g from the contact plane bridges the gap between them. With the above definition, Eq. (13) is modified as

$$\frac{dj_b}{ds} + v_\alpha n_\alpha + \dot{g} = 0 , \tag{A2}$$

where $j_b(s)$ is the flux on the contact areas measured as a function of s and is positive if the mass flow is along the direction of increasing s. In Fig. 3, $j_b > 0$ if the flow is from B to C and from D to E.

Integrating the above equation with $j_b(s_B) = 0$, one can express the flux on BC as

$$j_b(s) = -\int_0^s v_\alpha(s') n_\alpha ds' - G_1(s) , \tag{A3}$$

where

$$G_1(s) = \int_0^s \frac{g(s')}{\Delta t} ds' \tag{A4}$$

and the subscript on G indicates that the integration is carried out over S_{b1}.

Since the flux is continuous at the junction of the contact areas and the pore surface, the flux on the pore surface is easily expressed as

$$j_p(s) = j_b(s_C) - \int_{s_C}^s v_\alpha(s') n_\alpha ds' . \tag{A5}$$

Similarly, the flux on S_{b2} is obtained as

$$j_b(s) = j_p(s_D) - \int_{s_D}^s v_\alpha(s') n_\alpha ds - G_2(s) . \tag{A6}$$

Following Needleman and Rice (1980), one can interpolate the velocity on the contact area and pore surface using piecewise linear functions as

$$v_\alpha = \sum_i v_\alpha^i \phi_i(s) , \tag{A7}$$

wherein i denotes the node number and the summation is carried out over all the nodes on $(S_{b1} + S_p + S_{b2})$, $\alpha = 1,2$ and ϕ_i has the familiar form

$$\phi_i(s) = \begin{Bmatrix} \dfrac{s - s_{i-1}}{s_i - s_{i-1}}, & s_{i-1} \le s < s_i \\ \dfrac{s_{i+1} - s}{s_{i+1} - s_i}, & s_i \le s < s_{i+1} \\ 0, & s < s_{i-1} \text{ or } s > s_{i+1} \end{Bmatrix}. \tag{A8}$$

The flux on the interfaces and the pore surface can now be calculated analytically in terms of the nodal velocities by introducing these velocity interpolation functions, (A8) into the flux integrals, Eqs. (A3), (A5), and (A6), and carrying out the integrations. If one defines m_α^i as

$$m_\alpha^i(s) = \int_0^s \phi_i(s') n_\alpha ds', \tag{A9}$$

then the flux on the interface and the pore surface can be generally expressed as

$$j(s) = -\sum_i m_\alpha^i(s) v_\alpha^i - G(s) \tag{A10}$$

and the function $G(s)$ is evaluated according to the relation

$$G(s) = \begin{Bmatrix} G_1(s), & s \le s_C \\ G_1(s_C), & s_C < s \le s_D \\ G_1(s_C) + G_2(s), & s > s_D \end{Bmatrix} \tag{A11}$$

In matrix notation,

$$j(s) = \{M(s)\}^T \{v^N\} - G(s), \tag{A12}$$

where $\{M(s)\}$ is a $2(|N_E - N_B| + 1) \times 1$ array whose entries are the terms $m_\alpha^i(s)$, $\{v^N\}$ is the array of nodal velocities on the surface $(S_{b1} + S_p + S_{b2})$ and N_E and N_B are the node numbers at the points E and B respectively.

If Δs is an infinitesimal segment of S_p, it can be readily shown by geometric argument that

$$k \delta u_n \Delta s = \delta(\Delta s) \tag{A13}$$

and thus,

$$\int_{S_p} \gamma_p k \delta v_n ds = \int_{S_p} \gamma_p \delta \dot{s} ds = \sum_{i=1}^{N_{el}^p} \gamma_p \delta \dot{l}_i, \tag{A14}$$

where N_{el}^p is the number of element sides on the pore surface and l_i is the length of the ith side. Here, it is to be noted that the lengths of the elements change solely due to the motion of the pore surface normal to itself.

In order to cast the above relation in terms of the virtual nodal velocities and displacement increments, consider the ith pore surface edge l^i defined by the nodes i and $i+1$. Let the angles that the tangents to the pore surface make with the x-axis at these nodes be θ^i and θ^{i+1} respectively at time t_n. Virtual velocities δv_x^i and δv_y^i act at

node i. Then, the virtual velocity along the direction normal to the pore surface pointing into the particle is

$$\delta v_n^i = -\delta v_x^i \sin\theta^i + \delta v_y^i \cos\theta^i . \tag{A15}$$

If one denotes the position at time t_{n+1} of node i by the vector X^i, then the new virtual position x^i due to its virtual motion in the normal direction is given by

$$\begin{aligned} x^i &= X^i + \delta v_n^i \Delta t\, n \\ &= X^i + \Delta t\,(-\delta v_x^i \sin\theta^i + \delta v_y^i \cos\theta^i)(-\sin\theta^i e_x + \cos\theta^i e_y) \\ &= X^i + \Delta t\left[(\delta v_x^i \sin^2\theta^i - \delta v_y^i \sin\theta^i \cos\theta^i)e_x + (-\delta v_x^i \sin\theta^i \cos\theta^i + \delta v_y^i \cos^2\theta^i)e_y\right] \end{aligned} \tag{A16}$$

where e_x and e_y are the Cartesian unit vectors.

Use of the shorthand $S^i = \sin\theta^i$ and $C^i = \cos\theta^i$ permits one to write

$$x^i = X^i + \Delta t\left[(\delta v_x^i (S^i)^2 - \delta v_y^i S^i C^i)e_x + (-\delta v_x^i S^i C^i + \delta v_y^i (C^i)^2)e_y\right] \tag{A17}$$

Similarly, for the node $i+1$ one obtains

$$x^{i+1} = X^{i+1} + \Delta t\left[(\delta v_x^{i+1} (S^{i+1})^2 - \delta v_y^{i+1} S^{i+1} C^{i+1})e_x + (-\delta v_x^{i+1} S^{i+1} C^{i+1} + \delta v_y^{i+1} (C^{i+1})^2)e_y\right] \tag{A18}$$

The new virtual length of the edge is the virtual distance between the two nodes after application of the virtual velocities, i.e.,

$$l_{new}^i = \left|(x^{i+1} - x^i)\right| \tag{A19}$$

Expressing the position vectors of the nodes at time t_{n+1} as $X^i = X^i e_x + Y^i e_y$ and $X^{i+1} = X^{i+1} e_x + Y^{i+1} e_y$ and neglecting terms that are $O(\Delta t^2)$, the new length of the edge can be shown to be

$$l_{new}^i = l_{old}^i \left[1 + \frac{\Delta t}{(l_{old}^i)^2}\begin{pmatrix}(X^{i+1} - X^i)(-\delta v_x^i (S^i)^2 + \delta v_y^i S^i C^i + \delta v_x^{i+1} (S^{i+1})^2 - \delta v_y^{i+1} S^{i+1} C^{i+1}) \\ -(Y^{i+1} - Y^i)(-\delta v_x^i S^i C^i + \delta v_y^i (C^i)^2 + \delta v_x^{i+1} S^{i+1} C^{i+1} - \delta v_y^{i+1} (C^{i+1})^2\end{pmatrix}\right] \tag{A20}$$

where $l_{old}^i = \left|(X^{i+1^i} - X^i)\right|$ is the length of the edge before application of the virtual velocities. With the new length thus defined, the virtual rate of change of edge length can be evaluated straightforwardly as $\delta \dot{l}_i = (l_{new}^i - l_{old}^i)/\Delta t$, which in conjunction with Eq. (A20) above can be written symbolically as

$$\delta \dot{l}_i = \{\delta v^N\}^T \{P\}, \tag{A21}$$

where $\{P\}$ and $\{\delta v^N\}$ are given by

$$\{P\} = \begin{Bmatrix} -(X^{i+1} - X^i)(S^i)^2 + (Y^{i+1} - Y^i)S^i C^i \\ (X^{i+1} - X^i)S^i C^i - (Y^{i+1} - Y^i)(C^i)^2 \\ (X^{i+1} - X^i)(S^{i+1})^2 - (Y^{i+1} - Y^i)S^{i+1} C^{i+1} \\ -(X^{i+1} - X^i)S^{i+1} C^{i+1} + (Y^{i+1} - Y^i)(C^{i+1})^2 \end{Bmatrix} \quad \text{and} \quad \{\delta v^N\} = \begin{Bmatrix} \delta v_x^i \\ \delta v_y^i \\ \delta v_x^{i+1} \\ \delta v_y^{i+1} \end{Bmatrix}. \tag{A22}$$

All the position coordinates in Eq. (A22) are those at time t_{n+1} and these can be related to the known position coordinates at time t_n through the displacement increments. If the corresponding coordinates at time t_n are denoted with the subscript n, then the following holds:

$$X^r = X_n^r + \Delta u_x^r, \quad \text{and} \quad Y^r = Y_n^r + \Delta u_y^r, \quad \text{for } r = i, i+1 \tag{A23}$$

Then, $\{P\}$ can be explicitly written as function of the displacement increments as

$$\{P\} = \begin{Bmatrix} -(X_n^{i+1} - X_n^i + \Delta u_x^{i+1} - \Delta u_x^i)(S^i)^2 + (Y_n^{i+1} - Y_n^i + \Delta u_y^{i+1} - \Delta u_y^i)S^i C^i \\ (X_n^{i+1} - X_n^i + \Delta u_x^{i+1} - \Delta u_x^i)S^i C^i - (Y_n^{i+1} - Y_n^i + \Delta u_y^{i+1} - \Delta u_y^i)(C^i)^2 \\ (X_n^{i+1} - X_n^i + \Delta u_x^{i+1} - \Delta u_x^i)(S^{i+1})^2 - (Y_n^{i+1} - Y_n^i + \Delta u_y^{i+1} - \Delta u_y^i)S^{i+1} C^{i+1} \\ -(X_n^{i+1} - X_n^i + \Delta u_x^{i+1} - \Delta u_x^i)S^{i+1} C^{i+1} + (Y_n^{i+1} - Y_n^i + \Delta u_y^{i+1} - \Delta u_y^i)(C^{i+1})^2 \end{Bmatrix}. \tag{A24}$$

Terms associated with changes in the areas of contact resulting from matter transport can be rewritten in matrix form following a similar procedure. Clearly, $(\delta v_{tip})_C = \delta v_x^C$ and the rate of change of the length of contact area BC is quite simply $(\delta v_x^C - \delta v_x^B)$. Since we are considering only one of the two contacting particles, $\dot{a}_1 = (\delta v_x^C - \delta v_x^B)/2$. Similarly, for the contact area DE, we get $(\delta v_{tip})_D = -\delta v_y^D$ and $\dot{a}_1 = -(\delta v_y^D - \delta v_y^E)/2$. Thus,

$$\begin{aligned} &\gamma_b \dot{a}_1 - \gamma_p (\delta v_{tip} \cos\phi)_C + \gamma_b \dot{a}_2 - \gamma_p (\delta v_{tip} \cos\phi)_D \\ &= \frac{1}{2}\gamma_b (\delta v_x^C - \delta v_x^B - \delta v_y^D + \delta v_y^E) - \gamma_p (\delta v_x^C \cos\phi_C - \delta v_y^D \cos\phi_D) \\ &= \{\delta v^N\}^T \{F_\gamma\}, \end{aligned} \tag{A25}$$

where

$$\{F_\gamma\} = \begin{Bmatrix} -\frac{1}{2}\gamma_b \\ \frac{1}{2}\gamma_b - \gamma_p \cos\phi_C \\ -\frac{1}{2}\gamma_b + \gamma_p \cos\phi_D \\ \frac{1}{2}\gamma_b \end{Bmatrix}. \tag{A26}$$

Setting $\{v^N\} = \{\Delta u^N\}/\Delta t$, and employing the standard interpolation matrices $[A]$ for the velocity and $[B]$ for the strain-rate inside the particle A, substitution of Eqs. (A12), (A22), and (A26) into the governing Eq. (20), yields the non-linear finite element equations

$$\int_A [B]^T \{\sigma\} dA + [K^d]\{\Delta u^N\} = \{F\}, \tag{A27}$$

where $[K^d]$ is the diffusion matrix given by

$$[K^d] = \frac{1}{\mathcal{D}_b \Delta t} \int_{S_b} \{M(s)\}\{M(s)\}^T ds \tag{A28}$$

and $\{F\}$ is the force vector defined as

$$\{F\} = \frac{1}{D_b}\int_{S_b} G(s)\{M(s)\}^T ds + \int_{S_T}[A]^T\{T\}ds - \sum_{i=1}^{N_{el}^P}\gamma_p\{P\} \\ -\{F_\gamma\} - \sigma_n(s_D)\{M(s_D)\} + \sigma_n(s_C)\{M(s_C)\}\,. \tag{A29}$$

All entities occurring in Eqs. (A27) are referred to time t_{n+1} and thus, Eqs. (A27) are also satisfied at this time.

A2. Solution

Upon setting

$$\{\mathcal{G}\} = \int_A [B]^T\{\sigma\}dA + [K^d]\{\Delta u^N\} - \{F\}\,, \tag{A30}$$

the finite element equations are stated as

$$\{\mathcal{G}\} = \{0\}\,. \tag{A31}$$

The stresses $\{\sigma\}$ at time t_{n+1} are calculated as $\{\sigma(t_{n+1})\} = \{\sigma(t_n)\} + \{\Delta\sigma\}$, where $\{\Delta\sigma\}$ depends on both the displacement and creep strain increments (see Appendix B). Thus, the set of equations (A31) has to be solved for both $\{\Delta u^N\}$ and $\{\Delta\varepsilon^c\}$ and since the creep strain increments are not known *a priori*, the solution procedure is iterative in nature.

Newton's iteration method is employed to solve Eqs. (A31). Each "global" iteration involves the solution of the following linearized equation for the correction $d\{\Delta u^N\}$ to the displacement increment $\{\Delta u^N\}$:

$$\{\mathcal{G}\} + \left[\frac{\partial\mathcal{G}}{\partial\Delta u^N}\right] d\{\Delta u^N\} = \{0\}\,, \tag{A32}$$

From the definition of $\{\mathcal{G}\}$, one obtains

$$\left[\frac{\partial\mathcal{G}}{\partial\Delta u^N}\right] = \int_A [B]^T\left[\frac{\partial(\Delta\sigma)}{\partial(\Delta\varepsilon)}\right][B]dA + \left[K^d\right] + \sum_{i=1}^{N_{el}^P}\gamma_p\left[\frac{\partial P}{\partial(\Delta u^N)}\right] + \\ \left[\frac{\partial F_\gamma}{\partial(\Delta u^N)}\right] + \{M(s_D)\}\left\{\frac{\partial\sigma_n(s_D)}{\partial(\Delta u^N)}\right\}^T - \{M(s_C)\}\left\{\frac{\partial\sigma_n(s_C)}{\partial(\Delta u^N)}\right\}^T\,, \tag{A33}$$

where $\left[\partial(\Delta\sigma)/\partial(\Delta\varepsilon)\right]$ depends on the values of stress $\{\sigma\}$ at time t_{n+1} and is calculated in Appendix B. During the iterations, only the force terms arising from the gap function and the external loads are independent of the deformation. All other terms present in $\{\mathcal{G}\}$ are functions of the current value of the nodal displacements at t_{n+1} and hence, give rise to derivatives with respect to $\{\Delta u^N\}$.

As seen from Eq. (A24), the components of $\{P\}$ are linear in the displacement increments and so, the matrix $\left[\partial P/\partial(\Delta u^N)\right]$ is calculated easily from that equation. On the other hand, the components of $\{F_\gamma\}$ depend on the displacements indirectly through $\cos\phi_C$ and $\cos\phi_D$ and therefore the computation of $\left[\partial F_\gamma/\partial(\Delta u^N)\right]$ entails that of the derivatives of $\cos\phi_C$ and $\cos\phi_D$. Similarly, the vectors $\left\{\partial\sigma_n(s_C)/\partial(\Delta u^N)\right\}$ and

$\{\partial\sigma_n(s_D)/\partial(\Delta u^N)\}$ are dependent on the displacements at time t_{n+1} and the method of calculating these are detailed later in the section.

In the following, the procedure for calculating $\cos\phi_C$ and $\cos\phi_D$ and their derivatives with respect to the displacement increments is discussed. Let $\mathbf{X}^C = X^C\mathbf{e}_x + Y^C\mathbf{e}_y$ be the position of the node occupying point C and $\mathbf{X}^{C+1} = X^{C+1}\mathbf{e}_x + Y^{C+1}\mathbf{e}_y$ that of the subsequent node on the pore at time t_{n+1}. Further, denote by ΔX the difference $X^{C+1} - X^C$ and by ΔY the difference $Y^{C+1} - Y^C$. Then, the length of the edge l_C at time t_{n+1} is $\sqrt{(\Delta X)^2 + (\Delta Y)^2}$ and $\cos\phi_C = \Delta X / l_C$. Suppose displacement increments $\Delta\mathbf{u}^C = \Delta u_x^C\mathbf{e}_x + \Delta u_y^C\mathbf{e}_y$ and $\Delta\mathbf{u}^{C+1} = \Delta u_x^{C+1}\mathbf{e}_x + \Delta u_y^{C+1}\mathbf{e}_y$ are applied to the two nodes respectively. Adopting a procedure similar to the one for calculating the vector $\{P\}$, we get value of ϕ_C at C:

$$\begin{aligned}\cos(\phi+\Delta\phi)_C &= \Delta X / l_C + \frac{1}{(l_C)^3}\begin{Bmatrix}-(\Delta Y)^2\\ \Delta X\,\Delta Y\\ (\Delta Y)^2\\ -\Delta X\,\Delta Y\end{Bmatrix}^T\begin{Bmatrix}\Delta u_x^C\\ \Delta u_y^C\\ \Delta u_x^{C+1}\\ \Delta u_y^{C+1}\end{Bmatrix}\\ &= \cos\phi_C + \frac{1}{(l_C)^3}\begin{Bmatrix}-(\Delta Y)^2\\ \Delta X\,\Delta Y\\ (\Delta Y)^2\\ -\Delta X\,\Delta Y\end{Bmatrix}^T\begin{Bmatrix}\Delta u_x^C\\ \Delta u_y^C\\ \Delta u_x^{C+1}\\ \Delta u_y^{C+1}\end{Bmatrix}\end{aligned} \tag{A34}$$

Similarly, if we denote the pore surface node nearest to the node occupying point D by the superscript $D-1$, we obtain the following relation for the dihedral angle at D:

$$\cos(\phi+\Delta\phi)_D = \cos\phi_D + \frac{1}{(l_D)^3}\begin{Bmatrix}-\Delta X\,\Delta Y\\ (\Delta X)^2\\ \Delta X\,\Delta Y\\ -(\Delta X)^2\end{Bmatrix}^T\begin{Bmatrix}\Delta u_x^D\\ \Delta u_y^D\\ \Delta u_x^{D-1}\\ \Delta u_y^{D-1}\end{Bmatrix} \tag{A35}$$

Evidently, the dependence of $\cos\phi_C$ and $\cos\phi_D$ on the displacement increments is linear and the derivatives $\{d(\cos\phi_C)/d(\Delta u^N)\}$ and $\{d(\cos\phi_D)/d(\Delta u^N)\}$ can be calculated by inspection.

The normal stresses at the tip are calculated numerically by averaging the values at the stations of integration of the element(s) surrounding it. If the tip node is the mid-side node of an element edge, then the relevant integration stations are confined within that element itself, whereas if the tip node is shared by two elements, each element contributes one integration station to the calculation of the normal stress. In the former case, the tip stress would depend on the 16 nodal displacement increments associated with the single element while in the latter all 26 nodal displacement increments from

the two elements would be involved in the computation. This procedure is extended to evaluate the stress derivatives in Eq. (A33) for nodes at C and D. A test value $u_t = 10^{-3}$ is assigned to one of the displacement increments Δu^i on which the tip stress depends, while all other nodal displacement increments are set to zero. The creep strains are retained at the levels dictated by the solution at time t_n and the resulting tip stress σ_n is calculated by the averaging procedure indicated above. The ratio (σ_n/u_t) of this computed tip stress to the test value is the required derivative of the tip stress with respect to the non-zero nodal displacement increment $(\partial\sigma_n/\partial\Delta u_i)$. This procedure is repeated for all the relevant degrees of freedom to give the entire matrix of tip stress derivatives.

Thus, all the quantities that are needed to calculate $\left[\partial \mathcal{G}/\partial\Delta u^N\right]$ and $\mathcal{G}$ are completely determined and Eq. (A32) is solved for $d\{\Delta u^N\}$. The displacement increment $\{\Delta u^N\}$ is updated by adding this correction to the existing value and a new value of the total strain increment $\{\Delta\varepsilon\} = [\mathrm{B}]\{\Delta u^N\}$ is obtained from this. The creep constitutive equations are then used to isolate the creep strain portion of this total strain increment. Calculation of this creep strain portion requires the solution of a system of 4 nonlinear equations at each integration station and the details of this "local" iterative scheme are presented in Appendix C.

A3. Constraint equations

As mentioned before, the finite element equations are to be solved under constraints imposed for the satisfaction of the flux-curvature and stress-curvature relations on the pore surface. Moreover, one also needs to satisfy the condition of zero flux at E. From the preceding formulation, the flux at point E has the form

$$j(s_E) = -\sum m_\alpha^i(s_E)v_\alpha^i - G_1(s_C) - G_2(s_E) \qquad \text{(A36)}$$

Since the velocities are approximated as the displacement increments divided by the time step, setting the flux at E equal to zero is easily achieved by imposing a constraint on the nodal displacement increments. This constraint involves all the nodes on the contact areas and the pore surface.

The curvature at any node on the pore surface at time t_{n+1} is calculated from nodal coordinates and is clearly dependent on the unknown displacement increments (see Appendix D). The curvature gradient at the midpoint of each two-noded element edge is calculated by a central difference scheme and the satisfaction of the flux-curvature relation at this point generates one constraint in terms of the displacement increments.

Finally, the stress-curvature relation on the pore surface is satisfied by generating and satisfying one constraint at each pore surface node (except the first and the last) such that at time t_{n+1}, the relation $\sigma_n = \gamma_p k$ is satisfied. It is seen that the satisfaction of a similar constraint at the first and last nodes leads to a deterioration of the quality of the numerical scheme and greater difficulty in achieving convergence. However, the

curvature values at the tip obtained from extrapolation agree very well with those obtained from the stress, as discussed in sections 5 and 6.

APPENDIX B: CALCULATION OF $[\partial(\Delta\sigma)/\partial(\Delta\varepsilon)]$

The finite element forms of constitutive Eqs. (3) and (6) are written respectively as

$$\{\sigma\} = [C^e]\{\varepsilon^e\} \tag{B1}$$

and

$$\{\dot{\varepsilon}^c\} = \{f(\{\sigma\})\} \tag{B2}$$

where $\{\sigma\}^{\mathrm{T}} = [\sigma_{11}, \sigma_{22}, \sigma_{33}, \sigma_{12}]$, $\{\varepsilon^e\}^{\mathrm{T}} = [\varepsilon^e_{11}, \varepsilon^e_{22}, \varepsilon^e_{33}, \varepsilon^e_{12}]$, and $\{\dot{\varepsilon}^c\}^{\mathrm{T}} = [\dot{\varepsilon}^c_{11}, \dot{\varepsilon}^c_{22}, \dot{\varepsilon}^c_{33}, \dot{\varepsilon}^c_{12}]$.

From equation (6), it is evident that for the isotropic case under plane strain conditions, $\{f\}$ takes the form

$$\{f\} = \begin{Bmatrix} 3C\sigma_e^n s_1/2 \\ 3C\sigma_e^n s_2/2 \\ 3C\sigma_e^n s_3/2 \\ 3C\sigma_e^n s_4 \end{Bmatrix} \tag{B3}$$

where the s_i (i = 1,4) are the deviatoric stresses defined as

$$\begin{aligned} s_1 &= \sigma_{11} - \sigma_{kk}/3\,, \\ s_2 &= \sigma_{22} - \sigma_{kk}/3\,, \\ s_3 &= \sigma_{33} - \sigma_{kk}/3\,, \\ s_4 &= \sigma_{12} \end{aligned} \tag{B4}$$

and $\sigma_e = \sqrt{3[s_1^2 + s_2^2 + s_3^2 + 2s_4^2]/2}$ is the equivalent stress.

Suppose the complete solution to the problem at time t_n is available and the solution at time t_{n+1} is required. Then,

$$\begin{aligned} \{\sigma(t_{n+1})\} &= \{\sigma(t_n)\} + \{\Delta\sigma\} \\ &= \{\sigma(t_n)\} + [C^e]\{\Delta\varepsilon^e\} \\ &= \{\sigma(t_n)\} + [C^e]\{\Delta\varepsilon\} - [C^e]\{\Delta\varepsilon^c\}\,. \end{aligned} \tag{B5}$$

Given $\{\Delta\varepsilon\}$, $\{\sigma(t)\} + [C^e]\{\Delta\varepsilon\}$ is completely determined and used as the elastic predictor $\{\sigma^e(t_{n+1})\}$. Thus, once $\{\Delta\varepsilon^c\}$ is known, stress $\{\sigma(t_{n+1})\}$ is calculated through

$$\{\sigma(t_{n+1})\} = \{\sigma^e(t_{n+1})\} - [C^e]\{\Delta\varepsilon^c\} \tag{B6}$$

For the creep strain increment $\{\Delta\varepsilon^c\}$, one obtains the approximation

$$\{\Delta\varepsilon^c\} = \{\dot{\varepsilon}^c\}\Delta t \tag{B7}$$

and the trapezoidal rule is used to calculate the strain rate

$$\{\dot{\varepsilon}^c\} = \frac{1}{2}\left[\{f(\{\sigma(t_n)\})\} + \{f(\{\sigma(t_{n+1})\})\}\right] \tag{B8}$$

Combining Eqs. (B7) and (B8), one gets the following implicit equation for the creep strain increments in terms of the time step Δt and the assumed total strain increment $\{\Delta\varepsilon\}$:

$$\{\Delta\varepsilon^c\} - \frac{1}{2}\Delta t\left[\{f(\{\sigma(t_n)\})\} + \{f(\{\sigma(t_{n+1})\})\}\right] = \{0\}. \tag{B9}$$

From Eqs. (B5), it follows that

$$\left[\frac{\partial(\Delta\sigma)}{\partial(\Delta\varepsilon)}\right] = [C^e] - [C^e]\left[\frac{\partial(\Delta\varepsilon^c)}{\partial(\Delta\varepsilon)}\right]. \tag{B10}$$

In order to evaluate the matrix of creep strain derivatives, one first obtains from Eqs. (B9),

$$\left[\frac{\partial(\Delta\varepsilon^c)}{\partial(\Delta\varepsilon)}\right] = \frac{1}{2}\Delta t\left[\frac{\partial f}{\partial\sigma}\right]\left[\frac{\partial(\Delta\sigma)}{\partial(\Delta\varepsilon)}\right], \tag{B11}$$

where the matrix of derivatives $\left[\partial f/\partial\sigma\right]$ are evaluated at time t_{n+1}. Thus, the unknown matrix of stress derivatives reappears on the right-hand side above and combining Eqs. (B10) and (B11) gives

$$\left[\frac{\partial(\Delta\sigma)}{\partial(\Delta\varepsilon)}\right] = [C^e] - \frac{1}{2}\Delta t[C^e]\left[\frac{\partial f}{\partial\sigma}\right]\left[\frac{\partial(\Delta\sigma)}{\partial(\Delta\varepsilon)}\right] \tag{B12}$$

which can be rearranged to yield

$$\left[\frac{\partial(\Delta\sigma)}{\partial(\Delta\varepsilon)}\right] = \left[[C^e]^{-1} + \frac{1}{2}\Delta t\left[\frac{\partial f}{\partial\sigma}\right]\right]^{-1} \tag{B13}$$

Carrying out a term by term differentiation of the vector $\{f\}$ in Eq. (B3), one gets the following expressions for the components of $\left[\partial f/\partial\sigma\right]$:

$$\frac{\partial f_i}{\partial\sigma_j} = \begin{Bmatrix} C\sigma_e^{n-1}[1+\frac{9}{4}(n-1)(\frac{s_i s_j}{\sigma_e^2})], & i=j=1,2,3 \\ 3C\sigma_e^{n-1}[1+3(n-1)(\frac{s_i s_j}{\sigma_e^2})], & i=j=4 \\ C\sigma_e^{n-1}[-\frac{1}{2}+\frac{9}{4}(n-1)(\frac{s_i s_j}{\sigma_e^2})], & i\neq j \;\&\; i,j=1,2,3 \\ \frac{9}{2}C\sigma_e^{n-1}(n-1)(\frac{s_i s_j}{\sigma_e^2}), & i=1,2,3 \;\&\; j=4 \end{Bmatrix}. \tag{B14}$$

Notice that

$$\frac{\partial f_i}{\partial\sigma_j} = \frac{\partial f_j}{\partial\sigma_i}. \tag{B15}$$

Thus, given the stress state from Eq. (B6), once $\{\Delta\varepsilon^c\}$ is determined as shown in Appendix C, Eqs. (B13) and (B14) in combination yield the matrix of derivatives $\left[\partial(\Delta\sigma)/\partial(\Delta\varepsilon)\right]$.

APPENDIX C: "LOCAL" ITERATIVE LOOP FOR THE CALCULATION OF $\{\Delta\varepsilon^c\}$ FROM $\{\Delta\varepsilon\}$

Eq. (B9) of Appendix B forms the basis for the calculation of the creep strain portion of the total strain increment $\{\Delta\varepsilon\} = [\mathrm{B}]\{\Delta u^N\}$. Defining

$$\{g(\Delta\varepsilon^c)\} = \{\Delta\varepsilon^c\} - \frac{1}{2}\Delta t\Big[\{f(\{\sigma(t_n)\})\} + \{f(\{\sigma^e(t_{n+1})\} - [C^e]\{\Delta\varepsilon^c\})\}\Big], \tag{C1}$$

one can cast Eq. (B9) as $\{g\} = \{0\}$, and this system of non-linear equations is solved for $\{\Delta\varepsilon^c\}$. The Newton iteration method is once again implemented at each station of integration in the bulk of the particles and this results in the solution of the linear system of equations:

$$\{g(\Delta\varepsilon^c)\} + \left[\frac{\partial g(\Delta\varepsilon^c)}{\partial(\Delta\varepsilon^c)}\right] d\{\Delta\varepsilon^c\} = \{0\} \tag{C2}$$

Upon differentiation of Eq. (C1), one obtains

$$\frac{\partial g_i(\Delta\varepsilon^c)}{\partial(\Delta\varepsilon_j^c)} = \frac{\partial(\Delta\varepsilon_j^c)}{\partial(\Delta\varepsilon_j^c)} - \frac{1}{2}\Delta t\frac{\partial f_i}{\partial\sigma_k}\frac{\partial(C_{kl}^e\Delta\varepsilon_l^c)}{\partial(\Delta\varepsilon_j^c)}. \tag{C3}$$

Once again, the derivatives $\partial f_i/\partial\sigma_k$ are evaluated at time t_{n+1}.

The three creep strains $\Delta\varepsilon_1^c$, $\Delta\varepsilon_2^c$ and $\Delta\varepsilon_3^c$ are not independent of each other; they are related through the incompressibility of creep deformation, i.e., $\Delta\varepsilon_1^c + \Delta\varepsilon_2^c + \Delta\varepsilon_3^c = 0$. Therefore, one needs to eliminate one of them from the above equations; for instance, one could set $\Delta\varepsilon_3^c = -(\Delta\varepsilon_1^c + \Delta\varepsilon_2^c)$ and eliminate $\Delta\varepsilon_3^c$. Then, for the plane strain case, with (k = 1,4),

$$\frac{\partial(C_{kl}^e\Delta\varepsilon_l^c)}{\partial(\Delta\varepsilon_j^c)} = \begin{Bmatrix} C_{kj}^e & j = 4 \\ C_{kj}^e - C_{k3}^e & j = 1,2 \end{Bmatrix} \tag{C4}$$

or, more generally,

$$\frac{\partial(C_{kl}^e\Delta\varepsilon_l^c)}{\partial(\Delta\varepsilon_j^c)} = C_{kj}^e - C_{k3}^e\delta_{1j} - C_{k3}^e\delta_{2j} \qquad j = 1,2,4 \tag{C5}$$

Thus, the tangent stiffness matrix for the local loop becomes

$$\frac{\partial g_i(\Delta\varepsilon^c)}{\partial(\Delta\varepsilon_j^c)} = \delta_{ij} + \frac{1}{2}\Delta t\frac{\partial f_i}{\partial\sigma_k}(C_{kj}^e - C_{k3}^e\delta_{1j} - C_{k3}^e\delta_{2j}) \tag{C6}$$

Here, the matrix on the left is a 3×3 matrix and the indices i and j take on values 1, 2 and 4 for stresses $\sigma_{11},\sigma_{22},\sigma_{12}$ and strains $\varepsilon_{11},\varepsilon_{22},\varepsilon_{12}$, whereas the index k runs from 1 through 4. With the tangent stiffness completely determined, Eqs. (C2) can now be solved to yield the correction $d\{\Delta\varepsilon^c\}$. The iterative procedure continues until the measure

$$e = \sqrt{\frac{d(\Delta\varepsilon_{ij}^c)d(\Delta\varepsilon_{ij}^c)}{\Delta\varepsilon_{ij}^c\Delta\varepsilon_{ij}^c}} \tag{C7}$$

falls below 2.5×10^{-4}.

APPENDIX D: CALCULATION THE PORE SURFACE CURVATURE

For all nodes on the pore surface except those at the tips, the curvature is determined by their position and those of their two closest neighbours. Denote by (x_{i-1}, y_{i-1}), (x_i, y_i) and (x_{i+1}, y_{i+1}) the position of nodes $(i-1)$, i and $(i+1)$ respectively. One can uniquely determine a circle of radius r centered at (a,b) passing through these three points, i.e., the three variables r, a and b can be obtained by solving the following system of equations:

$$\begin{aligned}(x_{i-1}-a)^2+(y_{i-1}-b)^2 &= r^2\\ (x_i-a)^2+(y_i-b)^2 &= r^2\\ (x_{i+1}-a)^2+(y_{i+1}-b)^2 &= r^2\end{aligned} \tag{D1}$$

The exact expressions for r, a and b have been obtained analytically in terms of the position coordinates; however, they are too cumbersome to report and one can state in symbolic terms

$$\begin{aligned}r &= r(x_{i-1}, y_{i-1}, x_i, y_i, x_{i+1}, y_{i+1})\\ a &= a(x_{i-1}, y_{i-1}, x_i, y_i, x_{i+1}, y_{i+1})\\ b &= b(x_{i-1}, y_{i-1}, x_i, y_i, x_{i+1}, y_{i+1}).\end{aligned} \tag{D2}$$

The reciprocal of the radius of the circle gives the curvature at node i, though due care should be given to the sign of the curvature. If the angle made with the x-axis by the chord joining nodes i and $(i-1)$ is less than that made by the chord joining nodes i and $(i+1)$, then the circle constructed as above is deemed convex with respect to the interior of the particle and the curvature is signed negative and vice versa.

$$k_i = k_i(x_{i-1}, y_{i-1}, x_i, y_i, x_{i+1}, y_{i+1}) = (\text{sign})\frac{1}{r(x_{i-1}, y_{i-1}, x_i, y_i, x_{i+1}, y_{i+1})} \tag{D3}$$

The curvature at time t_{n+1} is calculated as the sum of the curvature at time t_n and an increment obtained from changes in nodal positions due to the addition of displacement increments. From Eq. (D3), this increment is

$$\Delta k_i = \sum_{j=i-1}^{i+1}\left(\frac{\partial k_i}{\partial x_j}\Delta u_x^j + \frac{\partial k_i}{\partial y_j}\Delta u_y^j\right). \tag{D4}$$

The required derivatives of k_i with respect to each of the six coordinates involved are calculated analytically from Eq. (D3). The curvature of the nodes at the tips of the pore is calculated by a quadratic extrapolation of the curvatures at the three adjacent pore surface nodes. Assigning the subscript 0 to the values at the tip and 1, 2 and 3 to those at the three neighboring nodes, one finds that the curvature at the tip takes the form

$$k_0 = As_0^2 + Bs_0 + C \tag{D5}$$

where the constants A, B and C satisfy the system of equations

$$\begin{bmatrix} s_1^2 & s_1 & 1\\ s_2^2 & s_2 & 1\\ s_3^2 & s_3 & 1\end{bmatrix}\begin{Bmatrix} A\\ B\\ C\end{Bmatrix} = \begin{Bmatrix} k_1\\ k_2\\ k_3\end{Bmatrix}. \tag{D6}$$

The curvature increments Δk_1, Δk_2 and Δk_3 are obtained as explained in the preceding paragraph and these increments in turn are used to calculate the increment to the tip curvature, i.e.,

$$\Delta k_0 = \sum_{j=1}^{3} \left\{ s_0^2 \left(\frac{\partial A}{\partial k_j}\right) \Delta k_j + s_0 \left(\frac{\partial B}{\partial k_j}\right) \Delta k_j + \left(\frac{\partial C}{\partial k_j}\right) \Delta k_j \right\} \tag{D7}$$

Once all curvature increments are calculated as functions of the displacement increments, the constraints discussed in Appendix A (Section A3) are generated and applied.

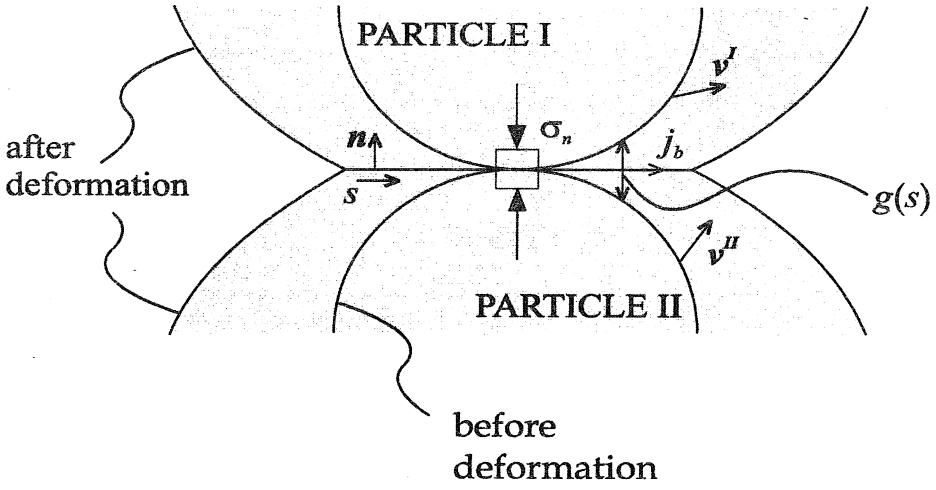

Fig. 1a. The interparticle contact area: s is the arclength, **n** is the unit normal vector, σ_n is the normal stress, j_b is the volumetric flux and $g(s)$ is the non-negative gap function.

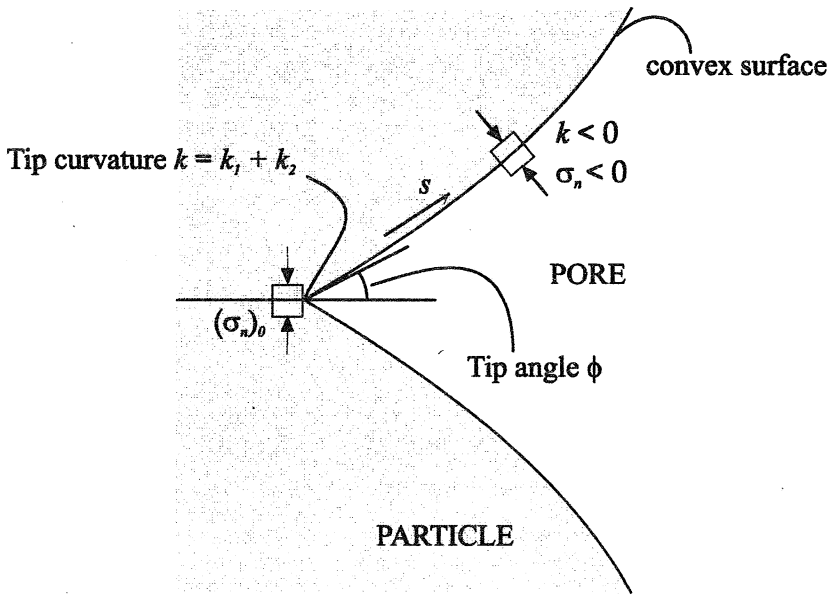

Fig. 1b. Sign convention for curvature on the pore surface: k is negative if the center of curvature is in the region occupied by the particle and correspondingly the stress is compressive.

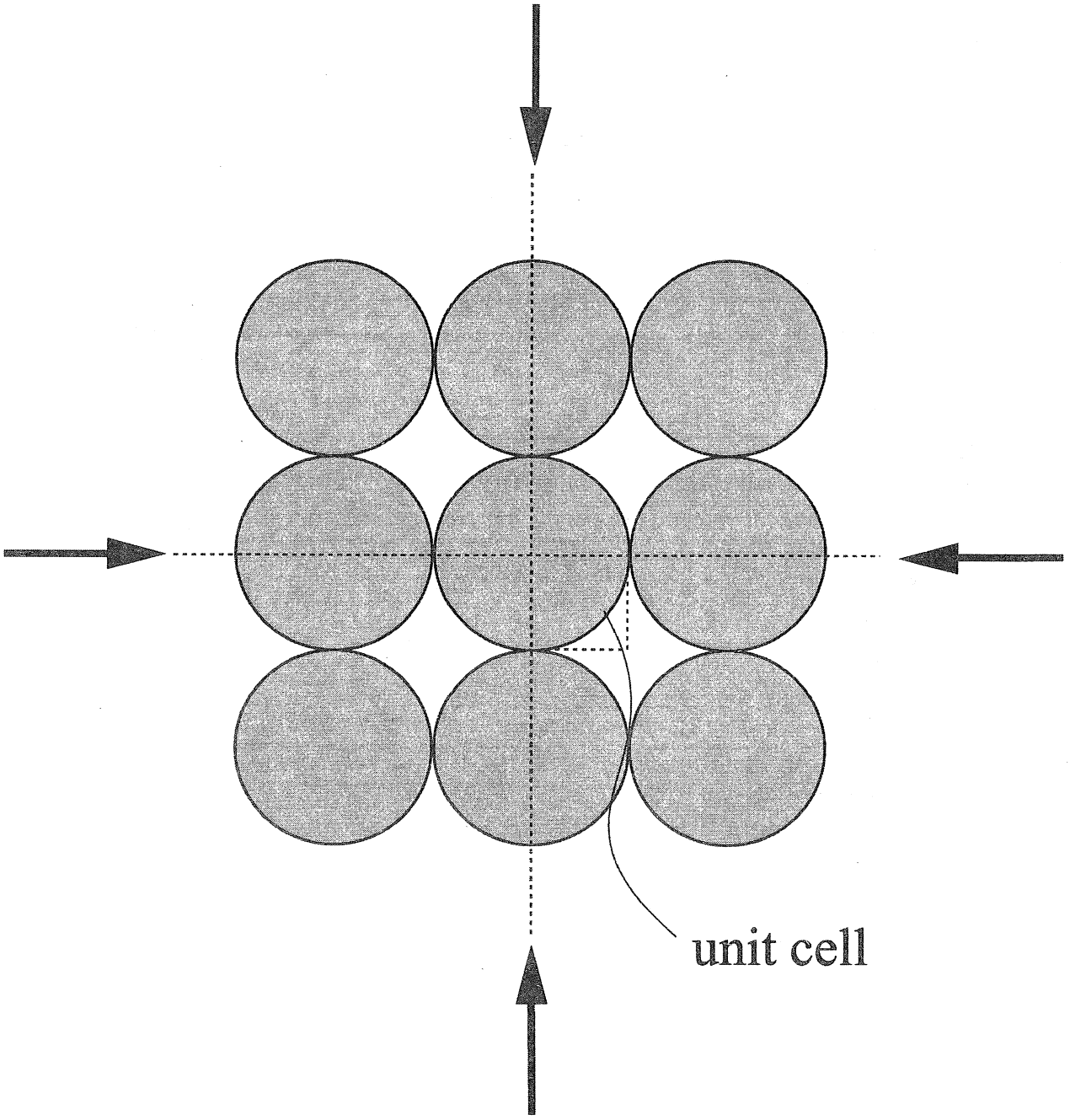

Fig. 2. Square arrangement of the powder particles under plane strain conditions. The square formed by the dashed lines is the unit cell chosen.

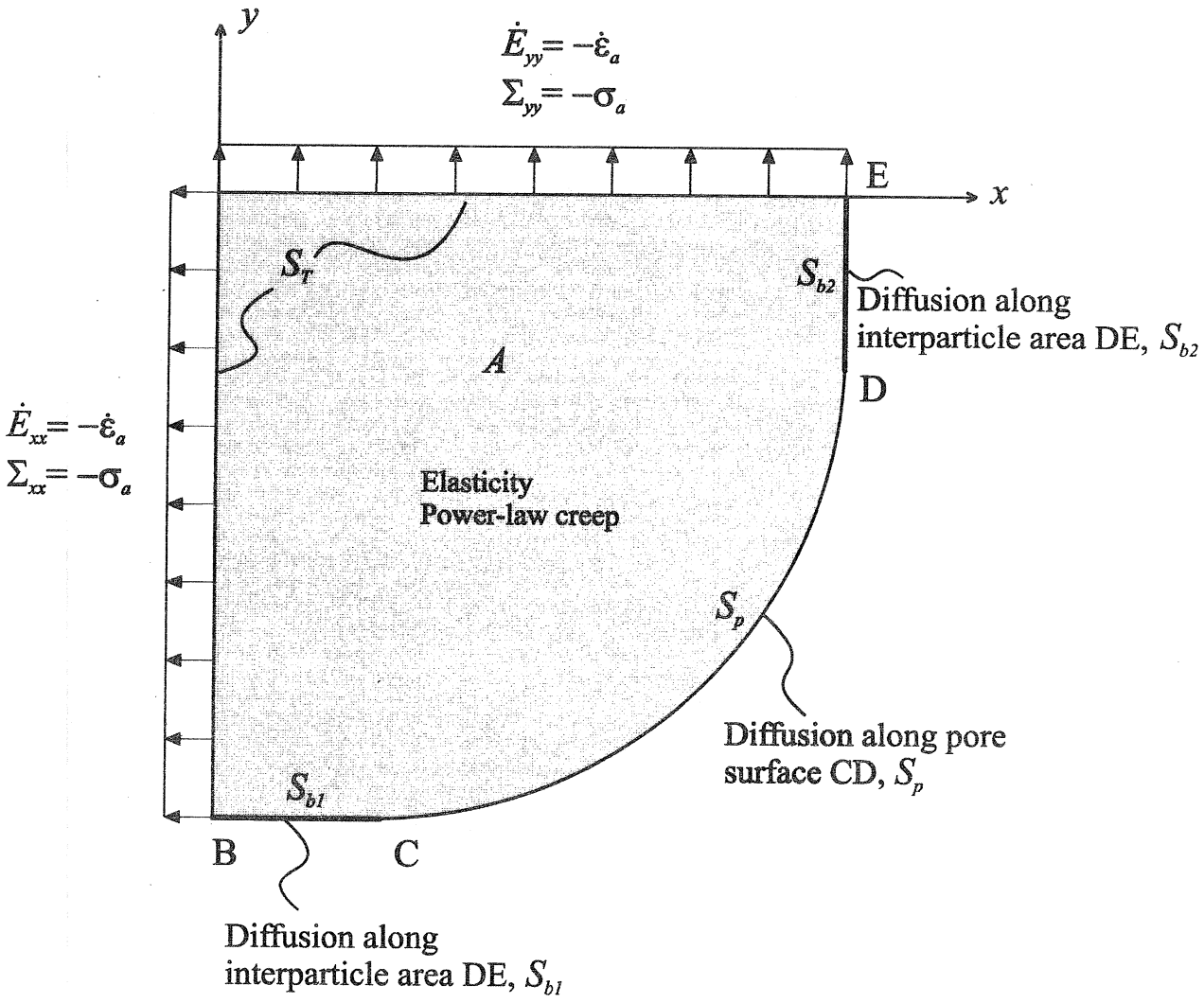

Fig. 3. Definition of the domains and boundary conditions on the unit cell.

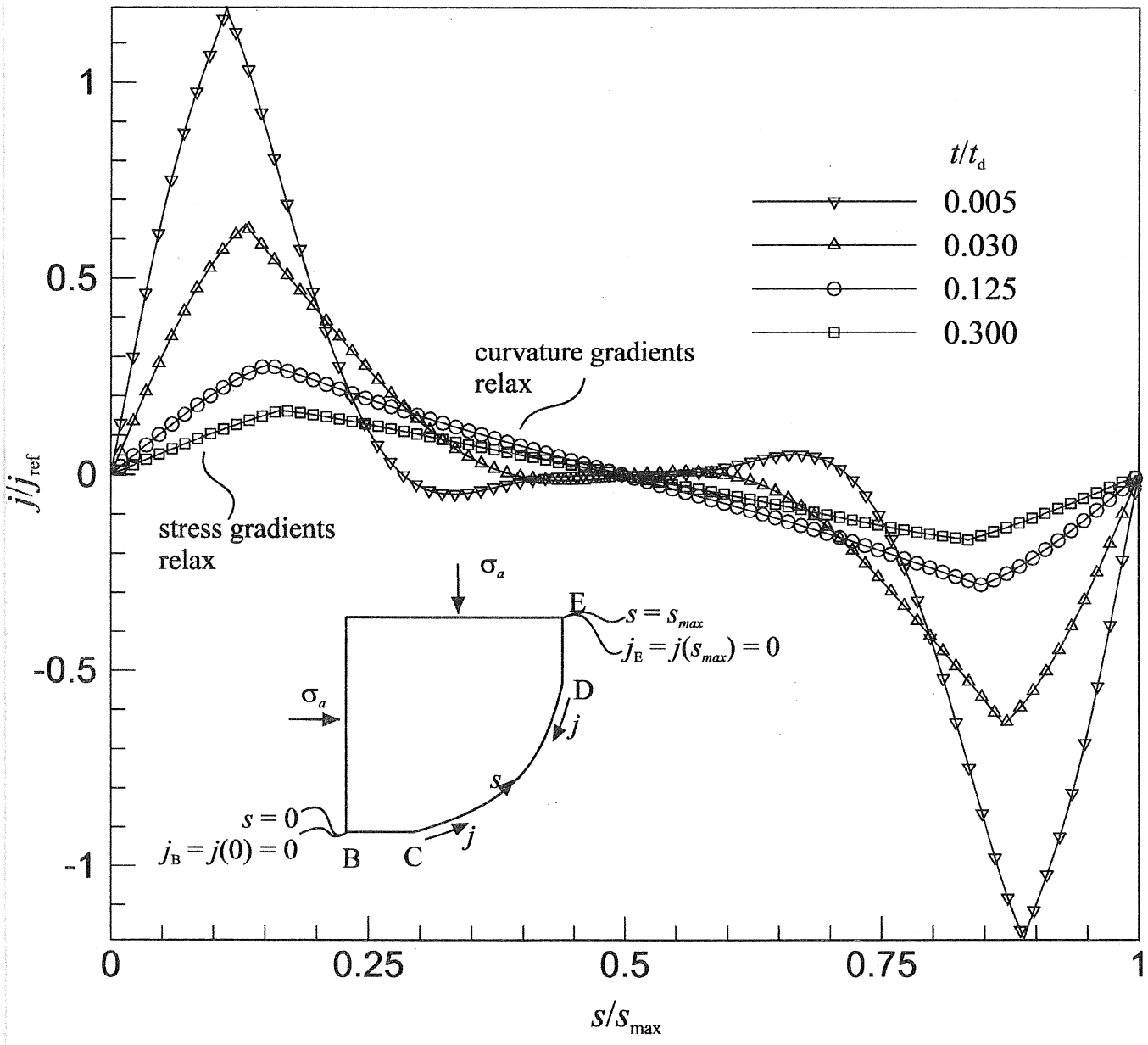

Fig. 4. Flux on the interparticle contact areas and pore surface for $\chi_b = 10$, $\chi_p = 100$, $\psi_b = \psi_p = 0.1$, $E/\sigma_a = 100$. Notice that $j = j_b$ on S_b and $j = j_p$ on S_p; $j_{ref} = \mathcal{D}_b \sigma_a / s_{max}$.

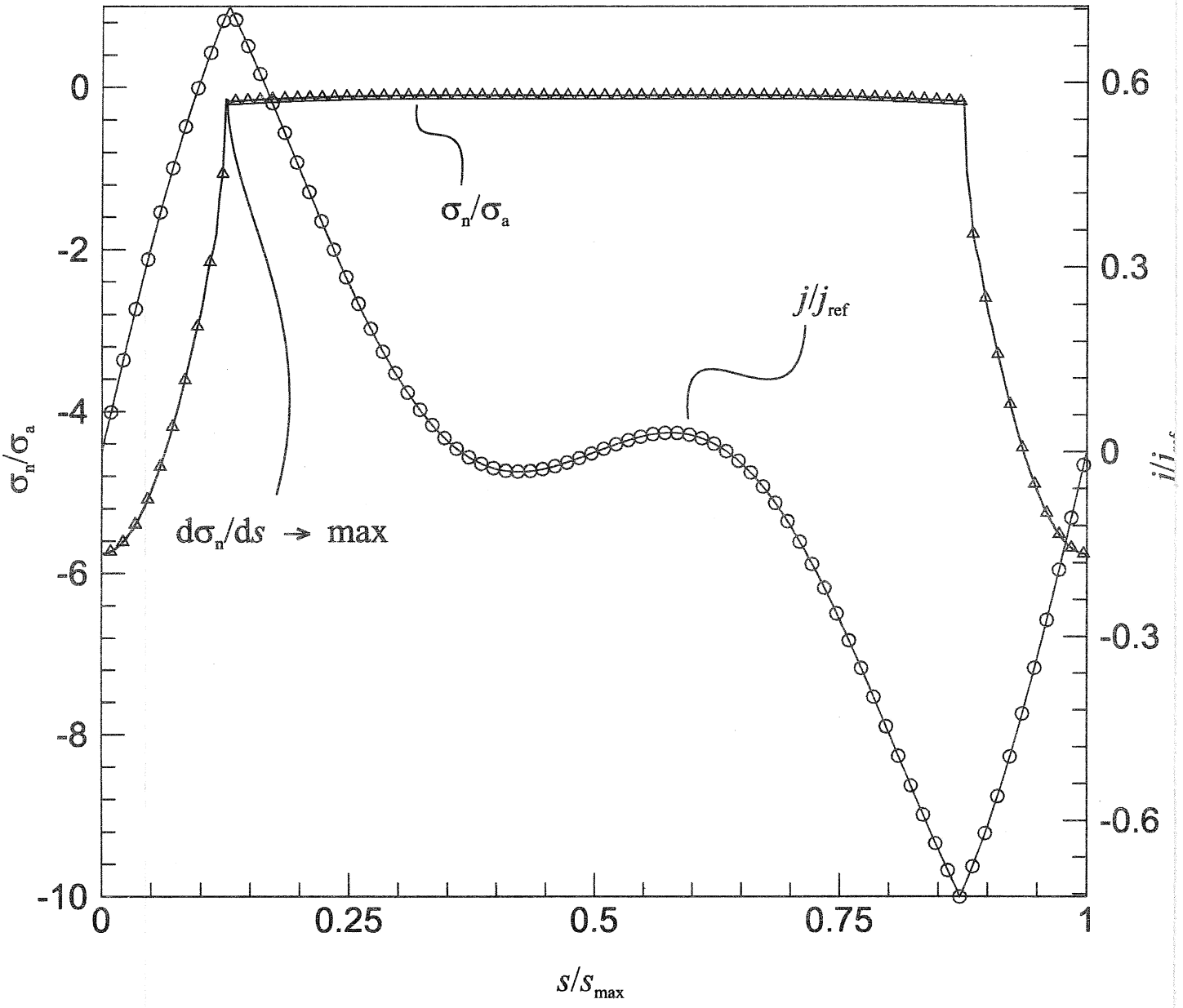

Fig. 5. Flux and normal stress on the interparticle contact areas and pore surface for $\chi_b = 10$, $\chi_p = 100$, $\psi_b = \psi_p = 0.1$, $E/\sigma_a = 100$ at time $t/t_d = 0.025$. Normalizing flux j_{ref} is equal to $\mathcal{D}_b \sigma_a / s_{max}$.

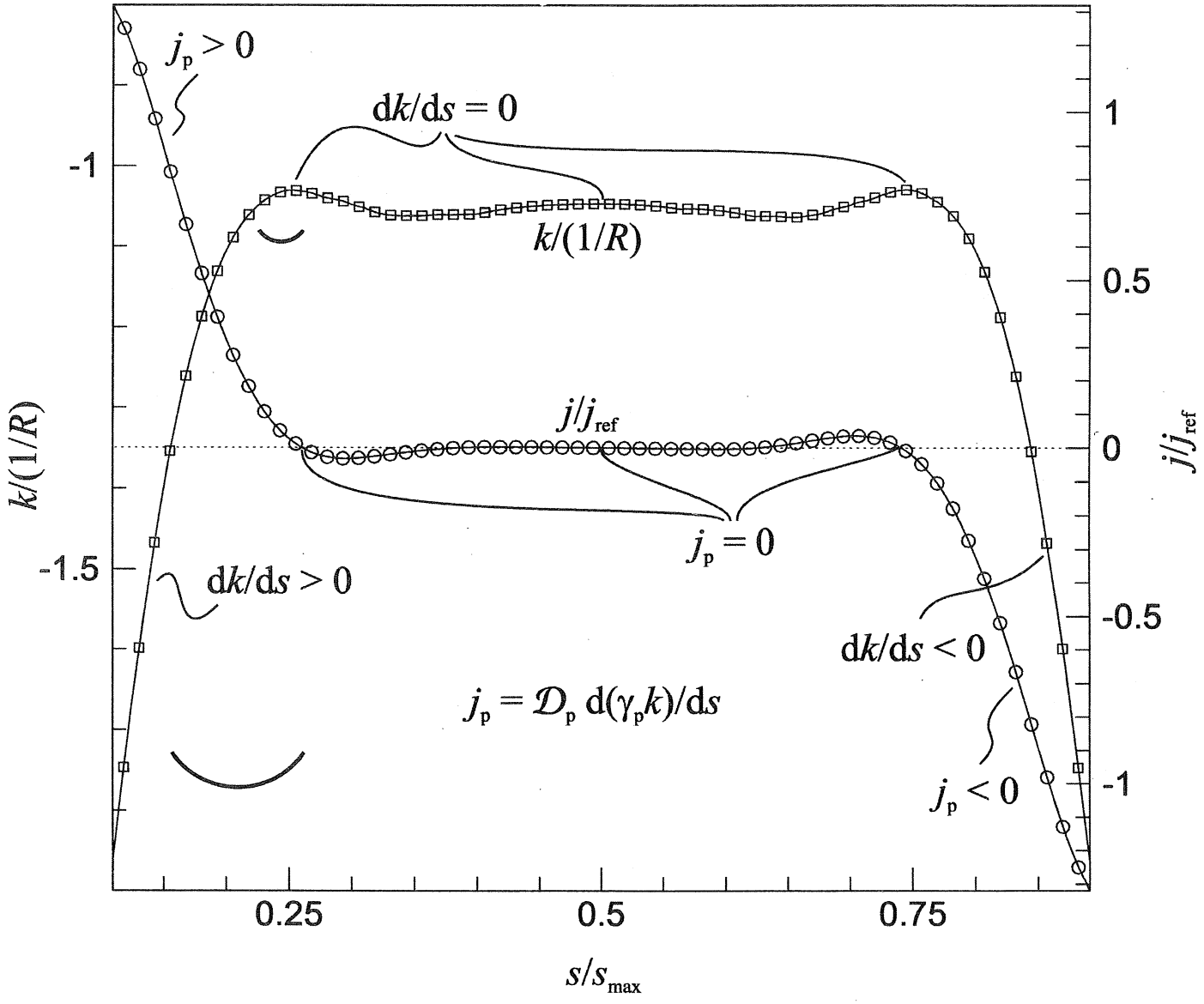

Fig. 6. Curvature and flux on the pore surface: $\chi_b = 10.$, $\chi_p = 100.$, $\psi_b = \psi_p = 0.1$, $E/\sigma_a = 100$ at time $t/t_d = 0.025$. Normalizing flux j_{ref} is equal to $\mathcal{D}_b \sigma_a / s_{max}$.

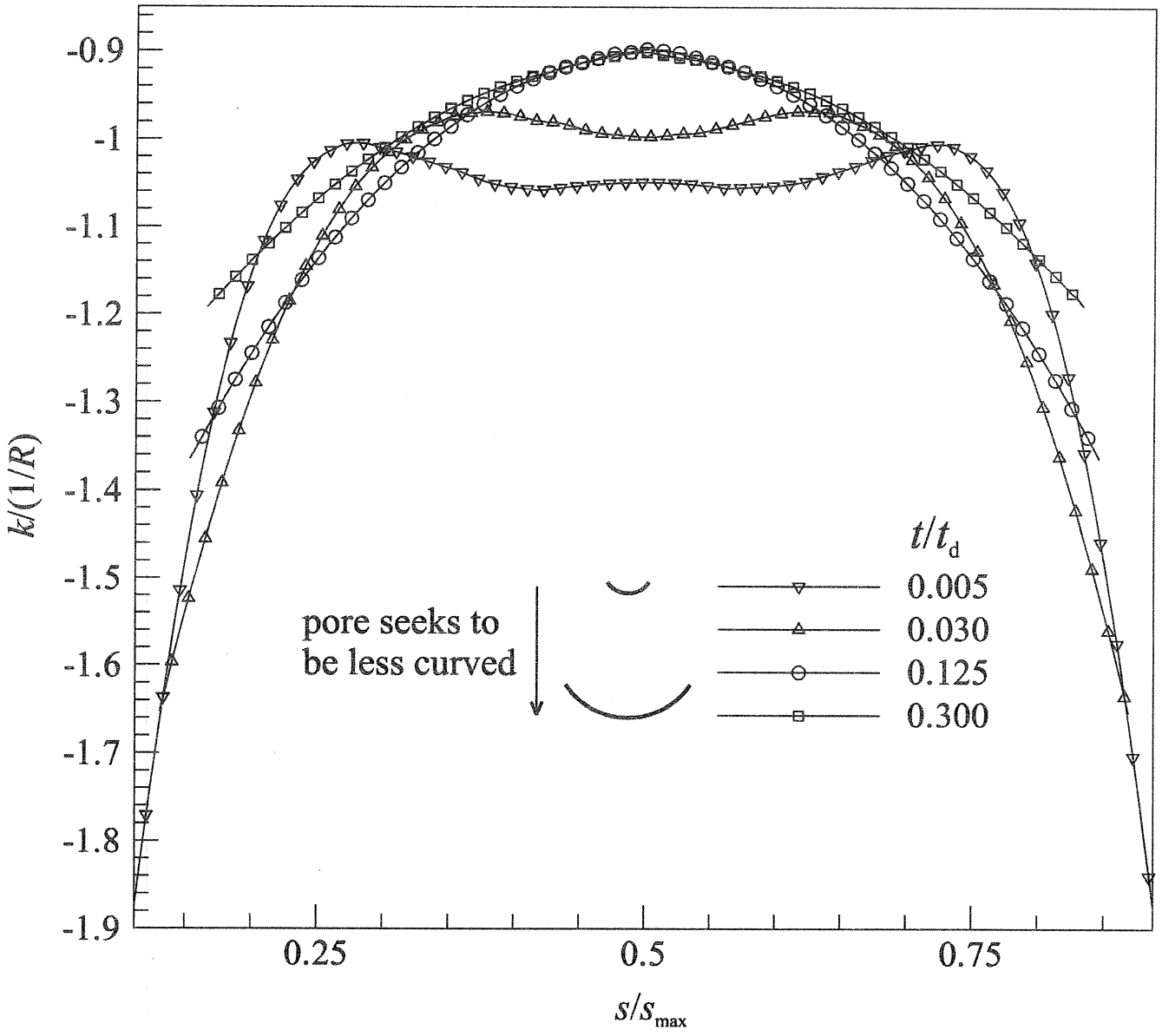

Fig. 7. Variation of pore surface curvature for $\chi_b = 10$, $\chi_p = 100$, $\psi_b = \psi_p = 0.1$, $E/\sigma_a = 100$.

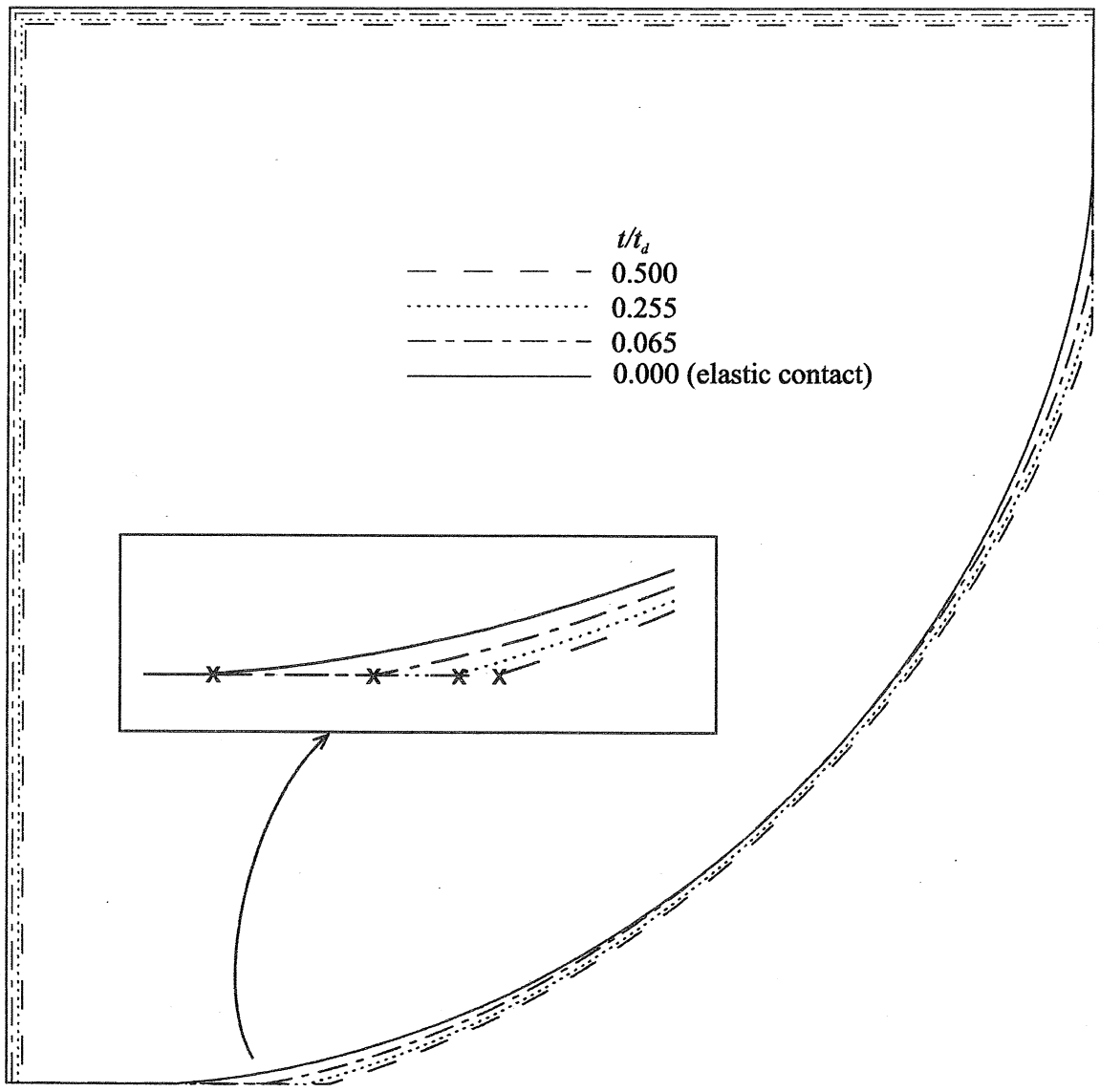

Fig. 8. Deformed mesh outlines at various times for $\chi_b = 10$, $\chi_p = 100$, $\psi_b = \psi_p = 0.1$, $E/\sigma_a = 100$. Sequential tip positions are shown in inset.

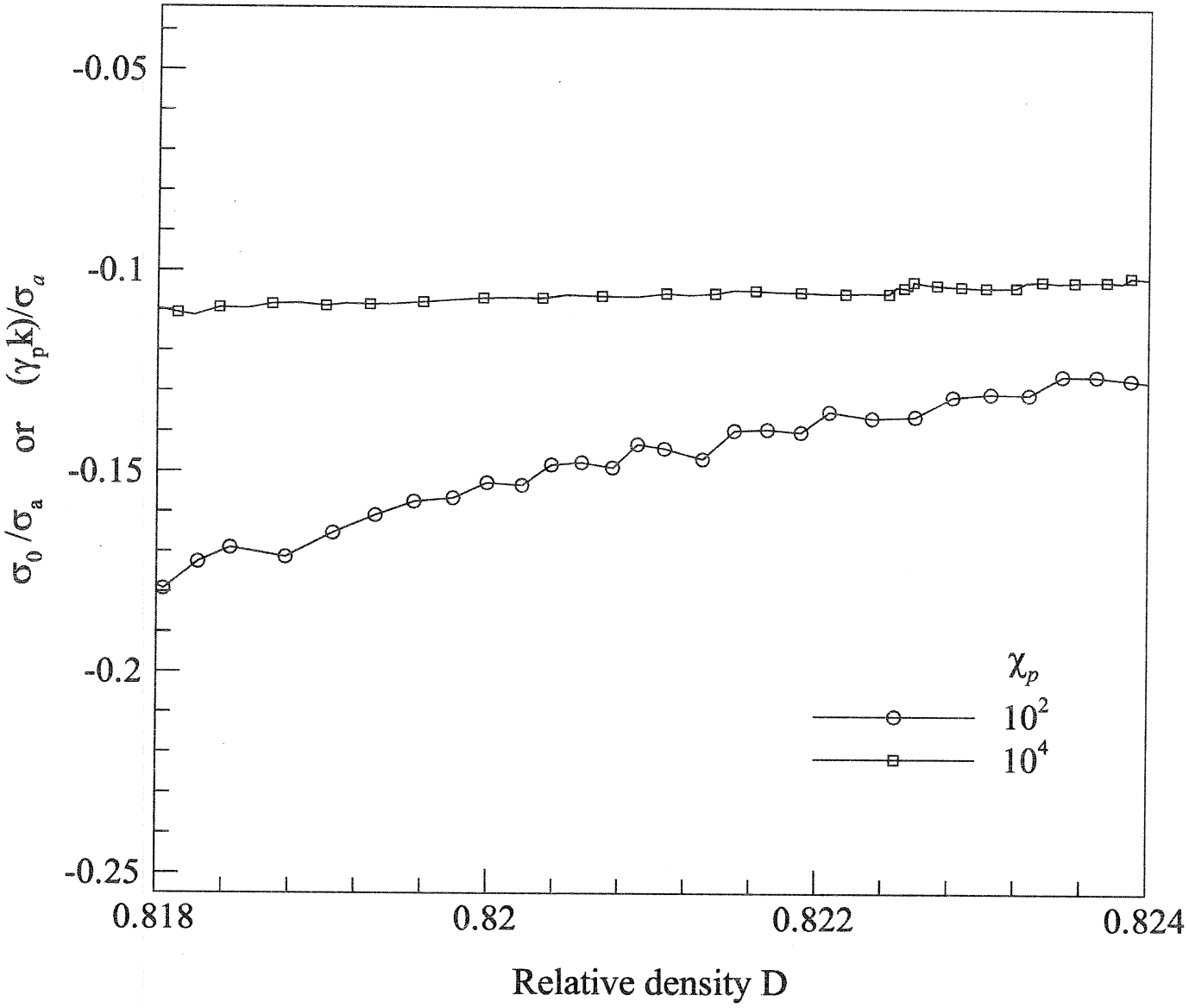

Fig. 9. Comparison of tip stresses for different surface diffusion parameters for $\chi_b = 10$, $\psi_b = \psi_p = 0.1$, $E/\sigma_a = 100$.

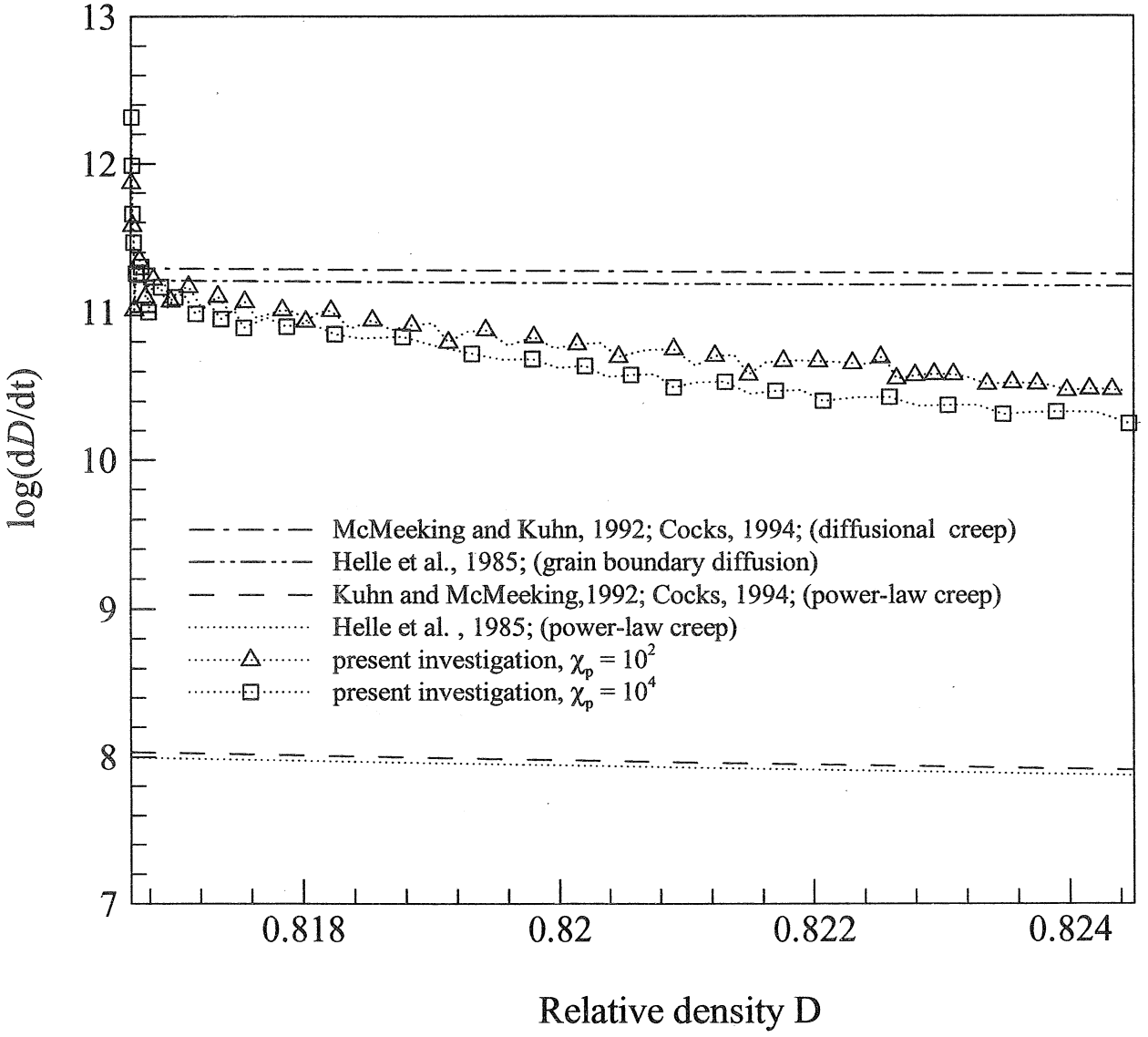

Fig. 10. Comparison of calculated densification rates with other analytical models.

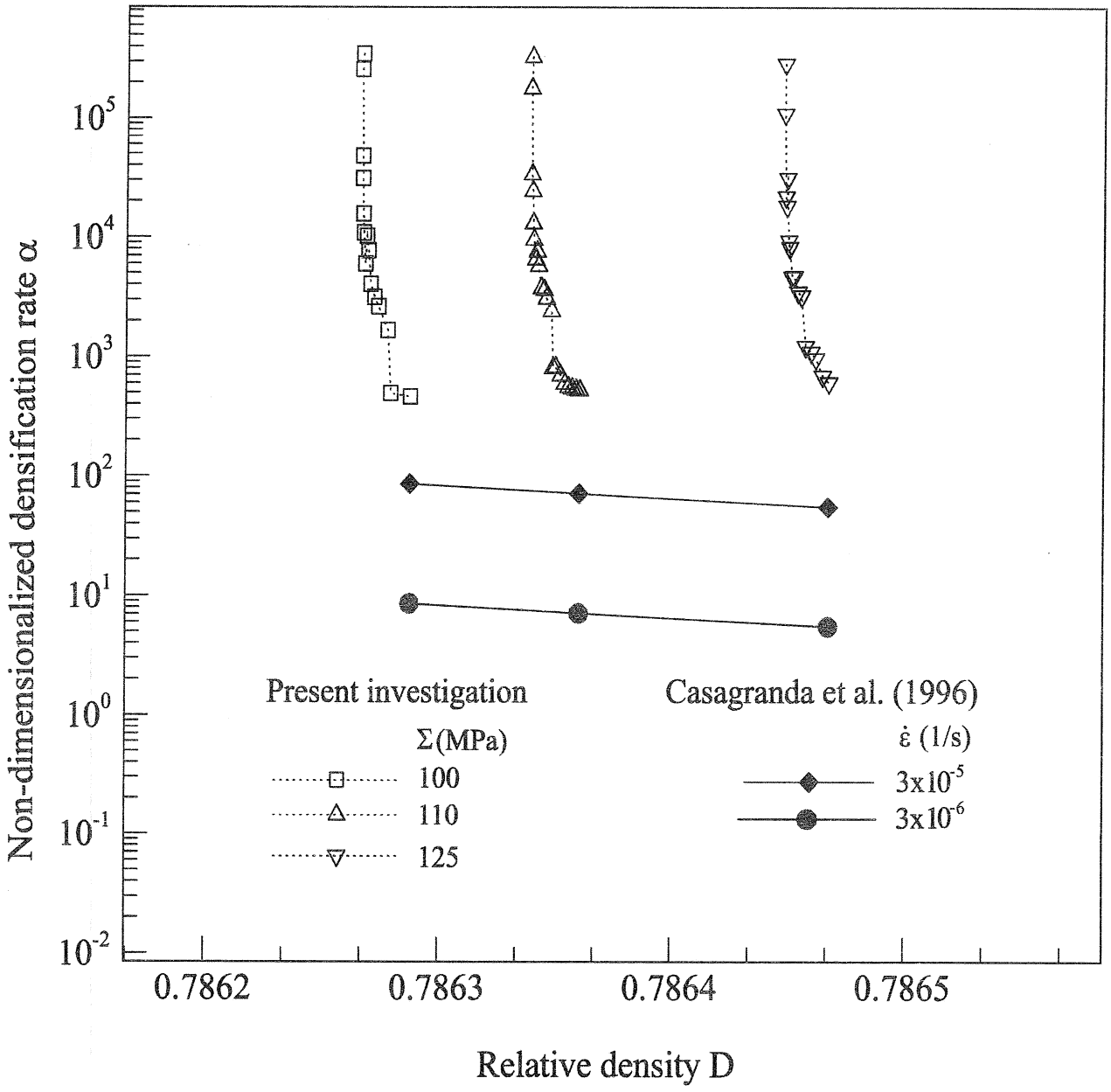

Fig. 11. Variation of consolidation rate with macroscopic stress (numerical calculations) and wi strain rate (experimental results) for Al_2O_3.

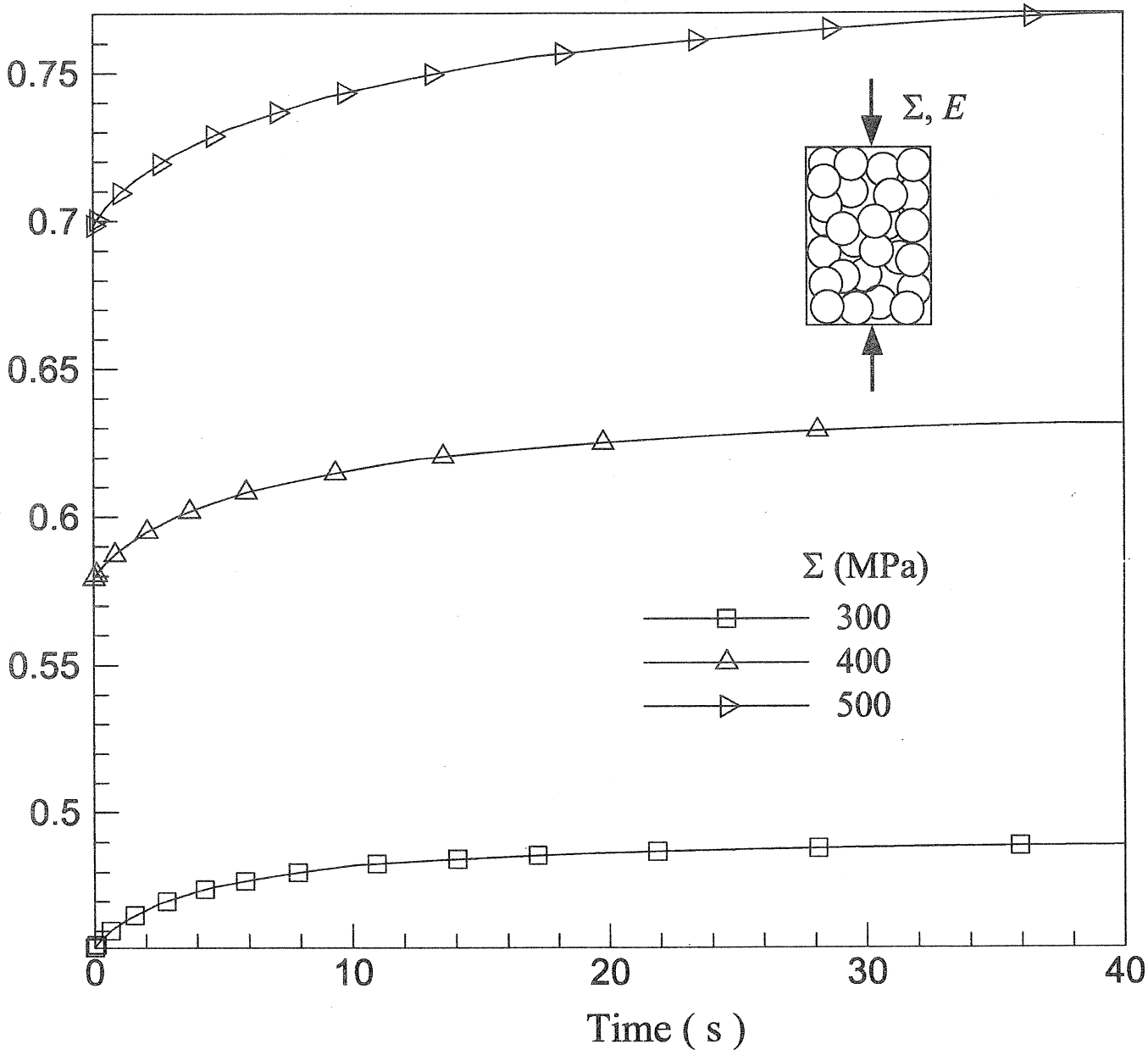

Fig. 12. Finite element calculation of uniaxial strain as a function of time for TiAl.

List of Recent TAM Reports

No.	Authors	Title	Date
817	Adrian, R. J.	Bibliography of particle velocimetry using imaging methods: 1917–1995—*Produced and distributed in cooperation with TSI, Inc., St. Paul, Minn.*	Mar. 1996
818	Fried, E., and G. Grach	An order-parameter based theory as a regularization of a sharp-interface theory for solid–solid phase transitions—*Archive for Rational Mechanics and Analysis* **138**, 355–404 (1997)	Mar. 1996
819	Vonderwell, M. P., and D. N. Riahi	Resonant instability mode triads in the compressible boundary-layer flow over a swept wing—*International Journal of Engineering Science* **36**, 599–624 (1998)	Mar. 1996
820	Short, M., and D. S. Stewart	Low-frequency two-dimensional linear instability of plane detonation—*Journal of Fluid Mechanics* **340**, 249–295 (1997)	Mar. 1996
821	Casagranda, A., and P. Sofronis	On the scaling laws for the consolidation of nanocrystalline powder compacts—Proceedings of the *IUTAM Symposium on the Mechanics of Granular and Porous Materials*, N. A. Fleck and A. C. F. Cocks, eds. The Netherlands: Kluwer Academic Publishers, 105–116 (1997)	Apr. 1996
822	Xu, S., and D. S. Stewart	Deflagration-to-detonation transition in porous energetic materials: A comparative model study—*Journal of Engineering Mathematics* **31**, 143–172 (1997)	Apr. 1996
823	Weaver, R. L.	Mean and mean-square responses of a prototypical master/fuzzy structure—*Journal of the Acoustical Society of America* **101**, 1441–1449 (1997)	Apr. 1996
824	Fried, E.	Correspondence between a phase-field theory and a sharp-interface theory for crystal growth—*Continuum Mechanics and Thermodynamics* **9**, 33–60 (1997)	Apr. 1996
825	Students in TAM 293–294	Thirty-third student symposium on engineering mechanics, J. W. Phillips, coordinator: Selected senior projects by W. J. Fortino II, A. A. Mordock, and M. R. Sawicki	May 1996
826	Riahi, D. N.	Effects of roughness on nonlinear stationary vortices in rotating disk flows—*Mathematical and Computer Modeling* **25**, 71–82 (1997)	June 1996
827	Riahi, D. N.	Nonlinear instabilities of shear flows over rough walls, *Far East Journal of Applied Mathematics*, in press (1998)	June 1996
828	Weaver, R. L.	Multiple scattering theory for a plate with sprung masses, mean responses—*Journal of the Acoustical Society of America* **101**, 3466–3414 (1997)	July 1996
829	Moser, R. D., M. M. Rogers, and D. W. Ewing	Self-similarity of time-evolving plane wakes *Journal of Fluid Mechanics*, in press (1998)	July 1996
830	Lufrano, J. M., and P. Sofronis	Enhanced hydrogen concentrations ahead of rounded notches and cracks: Competition between plastic strain and hydrostatic stress—*Acta Metallurgica et Materialia*, in press (1998)	July 1996
831	Riahi, D. N.	Effects of surface corrugation on primary instability modes in wall-bounded shear flows	Aug. 1996
832	Bechel, V. T., and N. R. Sottos	Application of debond length measurements to examine the mechanics of fiber pushout	Aug. 1996
833	Riahi, D. N.	Effect of centrifugal and Coriolis forces on chimney convection during alloy solidification—*Journal of Crystal Growth* **179** , 287–296 (1997)	Sept. 1996
834	Cermelli, P., and E. Fried	The influence of inertia on configurational forces in a deformable solid—*Proceedings of the Royal Society of London A* **453**, 1915–1927 (1997)	Oct. 1996
835	Riahi, D. N.	On the stability of shear flows with combined temporal and spatial imperfections	Oct. 1996
836	Carranza, F. L., B. Fang, and R. B. Haber	An adaptive space–time finite element model for oxidation-driven fracture, *Computer Methods in Applied Mechanics and Engineering*, in press (1997)	Nov. 1996

List of Recent TAM Reports (cont'd)

No.	Authors	Title	Date
837	Carranza, F. L., B. Fang, and R. B. Haber	A moving cohesive interface model for fracture in creeping materials, *Computational Mechanics* **19**, 517–521 (1997)	Nov. 1996
838	Balachandar, S., R. Mittal, and F. M. Najjar	Properties of the mean wake recirculation region in two-dimensional bluff body wakes—*Journal of Fluid Mechanics*, in press (1997)	Dec. 1996
839	Ti, B. W., W. D. O'Brien, Jr., and J. G. Harris	Measurements of coupled Rayleigh wave propagation in an elastic plate—*Journal of the Acoustical Society of America* **102**, 1528–1531	Dec. 1996
840	Phillips, W. R. C.	On finite-amplitude rotational waves in viscous shear flows—*Studies in Applied Mathematics* **100**, in press (1998)	Jan. 1997
841	Riahi, D. N.	Direct resonance analysis and modeling for a turbulent boundary layer over a corrugated surface—*Acta Mechanica*, in press (1998)	Jan. 1997
842	Liu, Z.-C., R. J. Adrian, C. D. Meinhart, and W. Lai	Structure of a turbulent boundary layer using a stereoscopic, large format video-PIV—*Developments in Laser Techniques and Fluid Mechanics*, 259–273 (1997)	Jan. 1997
843	Fang, B., F. L. Carranza, and R. B. Haber	An adaptive discontinuous Galerkin method for viscoplastic analysis—*Computer Methods in Applied Mechanics and Engineering* **150**, 191–198 (1997)	Jan. 1997
844	Xu, S., T. D. Aslam, and D. S. Stewart	High-resolution numerical simulation of ideal and non-ideal compressible reacting flows with embedded internal boundaries—*Combustion Theory and Modeling* **1**, 113–142 (1997)	Jan. 1997
845	Zhou, J., C. D. Meinhart, S. Balachandar, and R. J. Adrian	Formation of coherent hairpin packets in wall turbulence—In *Self-Sustaining Mechanisms in Wall Turbulence*, R. L. Panton, ed. Southampton, UK: Computational Mechanics Publications, 109–134 (1997)	Feb. 1997
846	Lufrano, J. M., P. Sofronis, and H. K. Birnbaum	Elastoplastically accommodated hydride formation and embrittlement—*Journal of Mechanics and Physics of Solids*, in press (1998)	Feb. 1997
847	Keane, R. D., N. Fujisawa, and R. J. Adrian	Unsteady non-penetrative thermal convection from non-uniform surfaces—In *Geophysical and Astrophysical Convection*, R. Kerr, ed. (1997)	Feb. 1997
848	Aref, H., and M. Brøns	On stagnation points and streamline topology in vortex flows—*Journal of Fluid Mechanics* **370**, 1–27 (1998)	Mar. 1997
849	Asghar, S., T. Hayat, and J. G. Harris	Diffraction by a slit in an infinite porous barrier—*Wave Motion*, in press (1998)	Mar. 1997
850	Shawki, T. G., H. Aref, and J. W. Phillips	Mechanics on the Web—Proceedings of the International Conference on Engineering Education (Aug. 1997, Chicago)	Apr. 1997
851	Stewart, D. S., and J. Yao	The normal detonation shock velocity–curvature relationship for materials with non-ideal equation of state and multiple turning points—*Combustion and Flame*, in press (1998)	Apr. 1997
852	Fried, E., A. Q. Shen, and S. T. Thoroddsen	Wave patterns in a thin layer of sand within a rotating horizontal cylinder—*Physics of Fluids* **10**, 10–12 (1998)	Apr. 1997
853	Boyland, P. L., H. Aref, and M. A. Stremler	Topological fluid mechanics of stirring	Apr. 1997
854	Parker, S. J., and S. Balachandar	Viscous and inviscid instabilities of flow along a streamwise corner—*Theoretical and Computational Fluid Dynamics*, in press (1997)	May 1997
855	Soloff, S. M., R. J. Adrian, and Z.-C. Liu	Distortion compensation for generalized stereoscopic particle image velocimetry—*Measurement Science and Technology* **8**, 1–14 (1997)	May 1997
856	Zhou, Z., R. J. Adrian, S. Balachandar, and T. M. Kendall	Mechanisms for generating coherent packets of hairpin vortices in near-wall turbulence—*Journal of Fluid Mechanics*, in press (1997)	June 1997
857	Neishtadt, A. I., D. L. Vainshtein, and A. A. Vasiliev	Chaotic advection in a cubic stokes flow—*Physica D* **111**, 227 (1997).	June 1997

List of Recent TAM Reports (cont'd)

No.	Authors	Title	Date
858	Weaver, R. L.	Ultrasonics in an aluminum foam—*Ultrasonics*, in press (1997)	July 1997
859	Riahi, D. N.	High gravity convection in a mushy layer during alloy solidification—In *Nonlinear Instability, Chaos and Turbulence*, D. N. Riahi and L. Debnath, eds., in press (1998)	July 1997
860	Najjar, F. M., and S. Balachandar	Low-frequency unsteadiness in the wake of a normal plate, *Journal of Fluid Mechanics*, in press (1997)	Aug. 1997
861	Short, M.	A parabolic linear evolution equation for cellular detonation instability	Aug. 1997
862	Short, M., and D. S. Stewart	Cellular detonation stability—I: A normal-mode linear analysis	Sept. 1997
863	Carranza, F. L., and R. B. Haber	A numerical study of intergranular fracture and oxygen embrittlement in an elastic–viscoplastic solid—*Journal of the Mechanics and Physics of Solids*, in press (1997)	Oct. 1997
864	Sakakibara, J., and R. J. Adrian	Whole-field measurement of temperature in water using two-color laser-induced fluorescence	Oct. 1997
865	Riahi, D. N.	Effect of surface corrugation on convection in a three-dimensional finite box of fluid-saturated porous material	Oct. 1997
866	Baker, C. F., and D. N. Riahi	Three-dimensional flow instabilities during alloy solidification	Oct. 1997
867	Fried, E.	Introduction (only) to *The Physical and Mathematical Foundations of the Continuum Theory of Evolving Phase Interfaces* (book containing 14 seminal papers dedicated to Morton E. Gurtin), Berlin: Springer-Verlag, in press (1998)	Oct. 1997
868	Folguera, A., and J. G. Harris	Coupled Rayleigh surface waves in a slowly varying elastic waveguide	Oct. 1997
869	Stewart, D. S.	Detonation shock dynamics: Application for precision cutting of metal with detonation waves	Oct. 1997
870	Shrotriya, P., and N. R. Sottos	Creep and relaxation behavior of woven glass/epoxy substrates for multilayer circuit board applications	Nov. 1997
871	Riahi, D. N.	Boundary wave–vortex interaction in channel flow at high Reynolds numbers, *Fluid Dynamics Research*, in press (1998)	Nov. 1997
872	George, W. K., L. Castillo, and M. Wosnik	A theory for turbulent pipe and channel flows—paper presented at *Disquisitiones Mechanicae* (Urbana, Ill., October 1996)	Nov. 1997
873	Aslam, T. D., and D. S. Stewart	Detonation shock dynamics and comparisons with direct numerical simulation	Dec. 1997
874	Short, M., and A. K. Kapila	Blow-up in semilinear parabolic equations with weak diffusion	Dec. 1997
875	Riahi, D. N.	Analysis and modeling for a turbulent convective plume—*Mathematical and Computer Modeling* **28**, 57–63 (1998)	Jan. 1998
876	Stremler, M. A., and H. Aref	Motion of three point vortices in a periodic parallelogram—*Journal of Fluid Mechanics*, in press (1999)	Feb. 1998
877	Dey, N., K. J. Hsia, and D. F. Socie	On the stress dependence of high-temperature static fatigue life of ceramics	Feb. 1998
878	Brown, E. N., and N. R. Sottos	Thermoelastic properties of plain weave composites for multilayer circuit board applications	Feb. 1998
879	Riahi, D. N.	On the effect of a corrugated boundary on convective motion	Feb. 1998
880	Riahi, D. N.	On a turbulent boundary layer flow over a moving wavy wall	Mar. 1998
881	Riahi, D. N.	Vortex formation and stability analysis for shear flows over combined spatially and temporally structured walls	June 1998
882	Short, M., and D. S. Stewart	The multi-dimensional stability of weak heat release detonations	June 1998
883	Fried, E., and M. E. Gurtin	Coherent solid-state phase transitions with atomic diffusion: A thermomechanical treatment—*Journal of Statistical Physics* (1998)	June 1998

List of Recent TAM Reports (cont'd)

No.	Authors	Title	Date
884	Langford, J. A., and R. D. Moser	Optimal large-eddy simulation formulations for isotropic turbulence	July 1998
885	Riahi, D. N.	Boundary-layer theory of magnetohydrodynamic turbulent convection—*Proceedings of the Indian National Academy (Physical Science)*, in press (1998)	Aug. 1998
886	Riahi, D. N.	Nonlinear thermal instability in spherical shells—in *Nonlinear Instability, Chaos and Turbulence* **2**, in press (1998)	Aug. 1998
887	Riahi, D. N.	Effects of rotation on fully non-axisymmetric chimney convection during alloy solidification	Sept. 1998
888	Fried, E., and S. Sellers	The Debye theory of rotary diffusion	Sept. 1998
889	Short, M., A. K. Kapila, and J. J. Quirk	The hydrodynamic mechanisms of pulsating detonation wave instability	Sept. 1998
890	Stewart, D. S.	The shock dynamics of multidimensional condensed and gas phase detonations	Sept. 1998
891	Kim, K. C., and R. J. Adrian	Very large-scale motion in the outer layer	Oct. 1998
892	Fujisawa, N., and R. J. Adrian	Three-dimensional temperature measurement in turbulent thermal convection by extended range scanning liquid crystal thermometry	Oct. 1998
893	Shen, A. Q., E. Fried, and S. T. Thoroddsen	Is segregation-by-particle-type a generic mechanism underlying finger formation at fronts of flowing granular media?	Oct. 1998
894	Shen, A. Q.	Mathematical and analog modeling of lava dome growth	Oct. 1998
895	Buckmaster, J. D., and M. Short	Cellular instabilities, sub-limit structures, and edge-flames in premixed counterflows	Oct. 1998
896	Harris, J. G.	*Elastic waves*—Part of a book to be published by Cambridge University Press	Dec. 1998
897	Paris, A. J., and G. A. Costello	Cord composite cylindrical shells	Dec. 1998
898	Students in TAM 293–294	Thirty-fourth student symposium on engineering mechanics (May 1997), J. W. Phillips, coordinator: Selected senior projects by M. R. Bracki, A. K. Davis, J. A. (Myers) Hommema, and P. D. Pattillo	Dec. 1998
899	Taha, A., and P. Sofronis	A micromechanics approach to the study of hydrogen transport and embrittlement	Jan. 1999
900	Ferney, B. D., and K. J. Hsia	The influence of multiple slip systems on the brittle–ductile transition in silicon	Feb. 1999
901	Fried, E., and A. Q. Shen	Supplemental relations at a phase interface across which the velocity and temperature jump	Mar. 1999
902	Paris, A. J., and G. A. Costello	Cord composite cylindrical shells: Multiple layers of cords at various angles to the shell axis	Apr. 1999
903	Ferney, B. D., M. R. DeVary, K. J. Hsia, and A. Needleman	Oscillatory crack growth in glass	Apr. 1999
904	Fried, E., and S. Sellers	Microforces and the theory of solute transport	Apr. 1999
905	Balachandar, S., J. D. Buckmaster, and M. Short	The generation of axial vorticity in solid-propellant rocket-motor flows	May 1999
906	Aref, H., and D. L. Vainchtein	The equation of state of a foam	May 1999
907	Subramanian, S. J., and P. Sofronis	Modeling of the interaction between densification mechanisms in powder compaction	May 1999